A model to predict surface gas transfer rate in streams based on turbulence production by aquatic vegetation

Chien-Yung Tseng[*,a], Rafael O. Tinoco[a]

[a]*Department of Civil and Environmental Engineering, University of Illinois at Urbana-Champaign, Urbana, IL, USA*
[*]*Corresponding Author, E-mail: cytseng2@illinois.edu*

Abstract

Turbulence generated by aquatic vegetation in lakes, estuaries, and rivers can significantly alter the flow structure throughout the entire water column, affecting gas transfer mechanisms at the air-water interface, thus modifying indicators of water quality. A series of laboratory experiments with rigid, acrylic cylinder arrays to mimic vegetation was conducted in a recirculating Odell-Kovasznay type race-track flume. Particle Image Velocimetry was used to characterize mean and turbulent flow statistics, to investigate the effect of emergent and submerged vegetation on gas transfer rate in terms of turbulent kinetic energy (TKE), Reynolds stresses, and TKE production. Surface gas transfer rates were determined by measuring dissolved oxygen concentration during re-aeration using an optical sensor. The results provided new insights on how stem- and canopy-scale turbulence affect the surface gas transfer rate at different submergence ratios and array densities. The relation between mean flow velocity and TKE production in each scenario is discussed, and a modified surface renewal model using TKE production as an indicator of gas transfer efficiency is developed to more accurately predict surface gas transfer rates in vegetated streams.

Preprint submitted to Advances in Water Resources *June 2, 2020*

Keywords: vegetated flows, turbulence production, gas transfer, surface renewal

1. Introduction

In natural water environments such as rivers, lakes, and estuaries, aquatic vegetation can significantly alter the mean and turbulent flow structure [27]. By changing water flow and generating turbulence, the presence of vegetation can also affect processes at the air-water interface and thus modify surface gas transfer mechanism [34, 8, 12] (Figure 1), which in turn affects practical management of water quality in aquatic environments. For example, installing aeration systems to enhance oxygen transfer to lakes and rivers with high biological oxygen demand (BOD) is one of the common ways that environmental engineers apply to keep an aquatic system well-aerated and prevent unpleasant algal blooms, hence maintaining adequate water quality to support other forms of aquatic life.

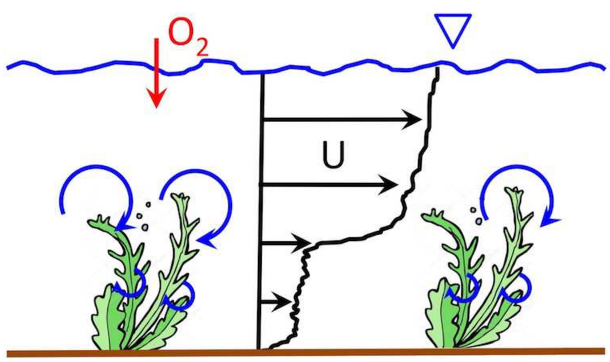

Figure 1: A schematic sketch showing the conceptual model of surface gas transfer mechanism affected by aquatic vegetation system.

Global warming depends on the transfer of greenhouse gasses (e.g., CO_2, CH_4) at the air-water surface. The conceptual model presented by the Intergovernmental Panel on Climate Change (IPCC) [35] considered only land and oceans as active boxes, connected by rivers acting as passive pipes. However, studies on stream metabolism and gas exchange [40, 13] have shown the active role of rivers in the exchange of carbon and oxygen through gas transfer at the air-water interface. Raymond and Cole [39] further pointed out a general lack of studies, physically-based predictive models, and direct measurement of gas transfer velocity in estuaries and rivers compared to the oceans. A better understanding of the magnitude and causes of variation in gas transfer velocity in rivers and estuaries is needed for estimating global mass balance of gases more accurately. It is one of the biggest sources of uncertainty in global warming models and a hot area of environmental fluid mechanics research. In order to address the needs and significances mentioned above, this study focuses on examining gas transfer rates in streams where aquatic vegetation exists from submerged to fully emergent.

In recent decades, there have been numerous models developed to study the gas transfer mechanism at the air-water interface [19]. Diffusive Boundary Layer (DBL) theory is the basis of most of the models, suggesting that the gas concentration gradient extends from the bulk concentration in water to the saturation concentration at the surface within a thin DBL. In the DBL, diffusive flux from air to water, F, follows Fick's law:

$$F = -D\frac{\partial C_w}{\partial z}\bigg|_{z=0}, \tag{1}$$

where D is the molecular diffusivity of water, C_w is the local concentration of dissolved oxygen (DO) in water, and $z = 0$ denotes the location at the air-water interface. Then F can be expressed as a function of the bulk concentration of DO, C_{DO}, in the water body using a gas transfer rate k_L:

$$F = k_L \left(C_{sat} - C_{DO}\right) , \tag{2}$$

where C_{sat} is the saturation concentration of DO in water. The gas transfer rate serves as the fundamental parameter for measuring the transfer velocity at which oxygen is entrained in water. Assuming that there are no losses of DO in water, and F is the only source transporting DO into the water column until DO reaches saturation ($C_{DO} = C_{sat}$), F can thus be rewritten as a time derivative form of the bulk concentration in water. The above equation can be further expressed as

$$F = H\frac{\partial C_{DO}}{\partial t} = k_L \left(C_{sat} - C_{DO}\right) , \tag{3}$$

where H is the averaged water depth. Solving the above first order ordinary differential equation with assumption of $C_{DO_{t=0}} = 0$, we obtain the solution of the bulk concentration of DO in water

$$C_{DO} = C_{sat}\left[1 - \exp\left(-\frac{1}{H}k_L t\right)\right] . \tag{4}$$

The DBL can be determined by the turbulence strength near the air-water interface. Danckwerts [5] first proposed a Surface Renewal (SR) model to estimate the interface gas transfer rate based on DBL theory and Higbie [11]'s penetration model. The model assumes that turbulent eddies can stochastically break through the liquid surface, carrying fresh parcels of fluid to the interface by molecular diffusion. The gas transfer rate, k_L, can be modeled by Poisson arrival times

$$k_L = \frac{1}{T_s}\int_0^{T_s} \exp(-t/T_s)\sqrt{\frac{D}{\pi t}}dt \approx \sqrt{\frac{D}{T_s}} , \tag{5}$$

where T_s is the SR time scale, which represents how long until the water parcel is replaced by a new fresh one.

Given the difficulty to measure T_s directly, many studies have proposed different methods to estimate it. Fortescue and Pearson [7] came up with a Large Eddy Surface Renewal (LESR) model arguing that the large eddies dominate the process of SR events, and the renewal time scale can be estimated by the bulk length scale, L, and the turbulence intensity, expressed as the root-mean-square of the velocity fluctuations in the bulk fluid, $\langle u' \rangle_{rms}$:

$$T_s \sim \frac{L}{\langle u' \rangle_{rms}} . \tag{6}$$

The angular brackets represent a time average, and u' represents velocity fluctuations using a typical Reynolds decomposition from the instantaneous velocity, u, and the time-averaged mean flow velocity, U, as:

$$u = U + u' . \tag{7}$$

Banerjee et al. [2] developed a Small Eddy Surface Renewal (SESR) model, which suggests that the renewal time scale is related to the turbulence intensity of small-scale eddies based on Kolmogorov time scale:

$$T_s \sim (\nu/\epsilon)^{1/2} , \tag{8}$$

where ν is the kinematic viscosity of water, and ϵ is the turbulent kinetic energy dissipation rate. Later on, Theofanous et al. [47] integrated both LESR and SESR models, and proposed a Two Regime Surface Renewal (TRSR) model based on turbulent Reynolds number defined as:

$$Re_t = \frac{\langle u' \rangle_{rms} L}{\nu} . \tag{9}$$

They argued that for $Re_t < 500$, large-scale eddies are dominant, while small-scale eddies are more representative of turbulent conditions for $Re_t > 500$. This yields a two regime prediction of the gas transfer rate:

$$k_L \sim \alpha Sc^{-1/2} \langle u' \rangle_{rms} {Re_t}^{-1/2}\,; \quad Re_t < 500\,, \tag{10}$$

$$k_L \sim \alpha Sc^{-1/2} \langle u' \rangle_{rms} {Re_t}^{-1/4}\,; \quad Re_t > 500\,, \tag{11}$$

where Sc is the Schmidt number ($Sc = \nu/D$), and α is the experimentally determined coefficient that depends on the flow condition. However, the aforementioned models rely on estimating the SR time scale, T_s. Instead of measuring it directly, there is a gap in the development of models that incorporate corrections for more complex conditions, such as vegetated flows.

McCready et al. [24] presented a relation between the divergence of the free surface velocity and the gas transfer process through the air-water interface. Banerjee [1] proposed a Surface Divergence (SD) model that directly relates the surface divergence velocity to the surface gas transfer rate:

$$k_L \sim c\sqrt{D \langle \beta \rangle_{rms}}\,, \tag{12}$$

where c is a coefficient that accounts for different flow conditions, and $\langle \beta \rangle_{rms}$ is the bulk root-mean-square of the divergence of surface fluctuations:

$$\langle \beta \rangle_{rms} = \sqrt{\langle \frac{\partial u'}{\partial x} + \frac{\partial v'}{\partial y} \rangle}\,. \tag{13}$$

The expression of Equation 12 is basically the same as Danckwerts [5] model for locally isotropic turbulence as discussed in Katul et al. [14]. However, compared to SR model, SD model eliminates the need to estimate T_s by introducing a new physical quantity, $\langle \beta \rangle_{rms}$, which can be directly measured in the field. Hence, SD model has been widely applied to different kinds of flows such as grid-stirred tank [25, 10], and open channel flows [45]. However, the functional form of the SD model still needs experiments to empirically define the coefficient c.

Turney and Banerjee [50] reviewed experimental results from previous studies and proposed a new version of the SD model that combines elements from both SR and SD theories. To adaptively estimate the gas transfer rate more specifically for rivers, Sanjou et al. [41] conducted a series of laboratory experiments to account for flow depth into the new modified SD model to take the bed-generated turbulence into consideration. However, the presence of vegetation in rivers makes the flows more complicated than non-vegetated open channel flows, where turbulence is mainly generated at the bed. The aforementioned past studies on prior development of gas transfer models in vegetation-free flow systems are summarized in Table 1.

Table 1: The past studies on prior development of gas transfer models in vegetation-free flow systems.

Publication	Sample approach	Model formulation	Gas transfer model
Danckwerts [5](1951)	theoretical approach	$k_L = \sqrt{D/T_s}$	SR
Fortescue and Pearson [7](1967)	grid apparatus flow	$k_L = \sqrt{D/T_s}$, $T_s \sim L/\langle u' \rangle_{rms}$	SR (large eddy)
Banerjee et al. [2](1968)	flow with wavy surface	$k_L = \sqrt{D/T_s}$, $T_s \sim \nu^{1/2}/\epsilon^{1/2}$	SR (small eddy)
Theofanous et al. [47](1976)	various flow type data	$k_L \sim \alpha Sc^{-1/2} \langle u' \rangle_{rms} {Re_t}^{-1/2}$	SR ($Re_t < 500$)
		$k_L \sim \alpha Sc^{-1/2} \langle u' \rangle_{rms} {Re_t}^{-1/4}$	SR ($Re_t > 500$)
McCready et al. [24](1986)	counter-current wind shear	$k_L \sim 0.71\sqrt{D\langle \beta \rangle_{rms}}$	SD
Tamburrino and Gulliver [45](2002)	open channel flow	$k_L \sim 0.24\sqrt{DS_{\beta_{max}}/u_{*cb}}$	SD in spectral domain
McKenna and McGillis [25](2004)	grid-stirred tank	$k_L \sim 0.50\sqrt{D\langle \beta \rangle_{rms}}$	SD
Herlina and Jirka [10](2008)	grid-stirred tank	$k_L \sim 0.33\sqrt{D\langle \beta \rangle_{rms}}$	SD
Turney and Banerjee [50](2013)	open channel flow with wind waves	$k_L \sim c\sqrt{D/T_s} e^{-2T_s \langle \beta \rangle_{rms}}$, $c = erf\left(1/\sqrt{2\langle \beta \rangle_{rms} T_s}\right)$	combined SR and SD
Sanjou et al. [41](2017)	open channel flow	$k_L \sim 0.89\sqrt{L^+ D\langle \beta \rangle_{rms}}$	modified SD

Aquatic plants are able to convert mean flow energy into turbulent kinetic energy (TKE) at the scales of stems, leafs, branches, and canopies based on flow and vegetation parameters, such as: volumetric frontal area, $a = d/\Delta s^2$, where d is the element diameter and Δs is the average spacing between elements; submergence ratio, h/H, where h is the height of the plant and H is the water depth; and mean flow velocity, U. Array density and submergence ratio are two critical factors to characterize vegetative patches [28]. From 1980 to 2000, many studies focused on unconfined canopy flow (deeply submerged vegetated flow) by investigating the shear layer turbulence and mixing in terrestrial boundary layer flow [42, 36, 37, 6]. These studies showed that the turbulent stress at the top of the canopy is the dominant driving force of the flow compared to a negligible streamwise pressure gradient within the canopy. Raupach and Shaw [38] studied the TKE production within the canopy, finding that if the turbulence generated by stem wakes is 100% converted from the mean flow, then stem-scale wake TKE production, P_w, can be expressed in terms of canopy drag as

$$P_w = \frac{1}{2} C_D a U^3 , \qquad (14)$$

where a is the volumetric frontal area of the canopy, and C_D is a drag coefficient.

In natural aquatic systems, however, shallow submergence ($h/H > 0.2$) and emergent conditions ($h/H = 1$) are more common due to the limitation of light penetration [27], which drove more studies focusing on these types of vegetated flows. Nepf [26] proposed a Reynolds number argument based on stem element diameter, d, to predict the dominance between turbulent diffusion and mechanical diffusion within the emergent canopy elements. In depth-limited vegetated flows, two distinct exchange regions can be identified by the flow structure and the shear layer formed on top of the canopy [29]: the vertical exchange zone where mean and turbulent flow structures are influenced by the shear layer, and the longitudinal exchange zone, where similarly to emergent conditions, flow is highly dependent on stem-vegetative drag. Ghisalberti and Nepf [9] studied the growth of the submerged canopy shear layer, finding that the shear layer becomes fully developed once the shear-layer-scale TKE is balanced by the TKE dissipation rate within the canopy. Lopez and Garcia [21] applied a $k-\epsilon$ turbulence numerical model to predict mean and turbulent flow quantities in depth-limited submerged vegetated flows by investigating the energy budget terms such as TKE production, TKE dissipation rate, and TKE transport, with an additional dispersive production term to account for the spatial correlation effect. However, most of studies ignored the dispersive term [17] whose contribution is generally less than 10% to the total production when array roughness density, ah, is not extremely sparse ($ah > 0.1$).

Up to date, few studies have focused on vegetation effects on the air-water interface, which is important for estimating the gas transfer rate in streams with aquatic plants. Compared to open channel flows, both SR and SD models need further studies to develop a new model for vegetated flows, to account for turbulence caused by the aquatic plant canopies. As mentioned, SD model can be used to estimate the gas transfer rate directly from free surface turbulence characteristics. SR model, however, is more intuitive since the SD formulation can actually be recovered back to the most basic SR form [5] with a clean relation between two experimental coefficients

α and c [14]. However, accurate prediction of hydrodynamics throughout the water column based on the free surface velocity statistics is still an open field of research (e.g., [22]). To understand the role of aquatic vegetation on such transfer mechanisms, we propose developing an adaptive SR model for vegetated flows, as a relatively direct way to link flow-vegetation interactions to surface gas transfer processes.

The objective of this study is to investigate the effects of turbulence generated by aquatic vegetation on surface gas transfer, and to propose a model to predict the transfer rate, k_L, by linking bulk flow turbulence to surface motions. In Section 2, we described our methodology, experimental setup, and measurement techniques. In Section 3, we present the experimental results of mean and turbulent velocity statistics, showing their effect on surface gas transfer rate at different submergence ratios and array densities. In Section 4, we show the relations between mean flow velocity and TKE production, and develop a new modified SR model using TKE production as an indicator of gas transfer efficiency.

2. Methods

2.1. Experimental setup

The experiment was conducted in an Odell-Kovasznay type flume [30] (Figure 2) at the Ecohydraulics and Ecomorphodynamics Laboratory (EEL), in Rantoul, IL. The straight test section of the flume is 2 m long, 0.15 m wide, and 0.6 m deep. The flow is driven by a rotating disk pump that generates shear under different rotational frequencies to accurately control flow speeds to mimic a uni-directional river flow. By uniformly distributing the disks through the whole depth of the flume, the disk pump is able to produce a uniform velocity profile with minimal disturbance to the flow, as water continues to recirculate in an essentially infinite loop. This design ensures the full development of the boundary layer and turbulence features in the Odell-Kovasznay flume. The flume is further designed to minimize the secondary flows generated in the bending section, which allows us to ideally investigate the vertical flow structures and turbulence characteristics through a 2D approach simply following the center line of the flume.

In the present experiments, the disk rotational frequency, ω, is controlled by an inverter whose frequency, f, is in a range between 10 Hz to 40 Hz, allowing for mean flow velocities up to 25 cm/s. The relation between ω and f is:

$$\omega \ (rpm) = 6.6 f \ \ (Hz) \, . \tag{15}$$

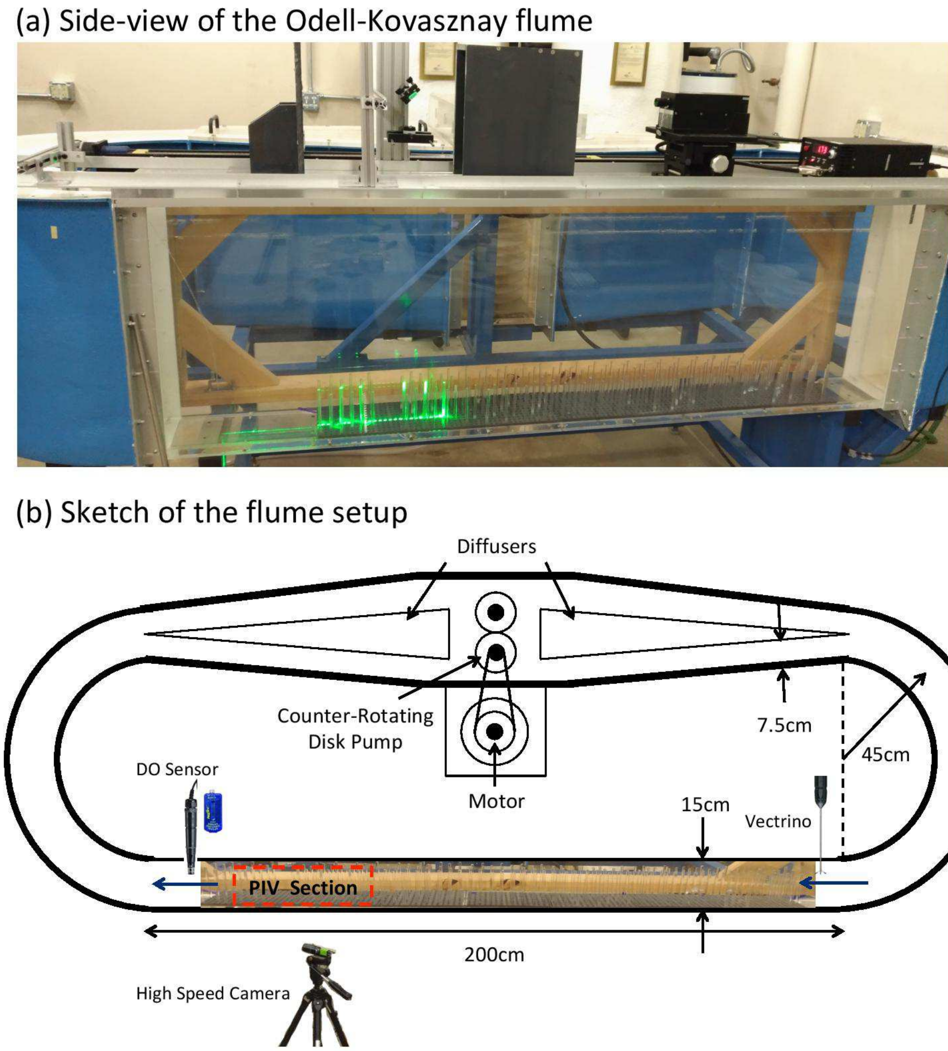

Figure 2: (a) Side view of the Odell-Kovasznay flume with laser setup for PIV. (b) Sketch of the flume showing the locations of the ADV on the upstream side of the straight test section, and the DO sensor on the downstream side to monitor re-aeration.

An array of rigid acrylic cylinders with diameter $d = 0.64\ cm$ and height $h = 10\ cm$ is used to simulate high-stiffness aquatic vegetation canopy, such as *Sagittaria sagittifolia* and *Sparganium erectum*, which are often found in vegetated streams. The vegetation array is 156.2 *cm* (246 *d*) long, and the leading edge is 20.3 *cm* (32 *d*) downstream from the beginning of the straight test section (Figure 3). A 7.6 *cm* (12 *d*) gap was created within the array from 135.3 *cm* to 142.9 *cm* (213 *d* to 225 *d*) from the beginning of the array for PIV. An Acoustic Doppler Velocimeter (ADV - Vectrino, Nortek) was put 8 *cm* upstream from the leading edge of the cylinder array with 10 vertical locations for calibration. The Dissolved Oxygen sensor (DO sensor - PASPORT Optical Dissolved Oxygen Sensor, PASCO), was put at the end of the straight test section of the flume near the water surface to monitor the DO concentration for estimating the gas transfer rate, k_L.

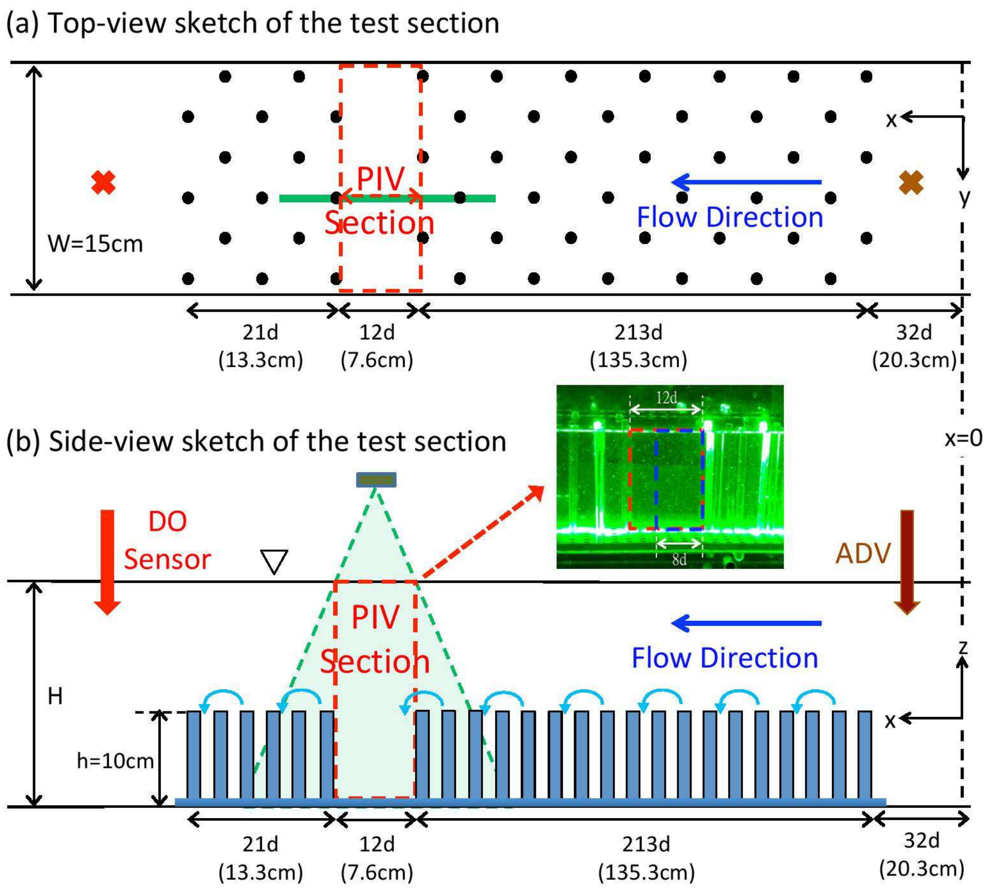

Figure 3: Top- (a) and side-view (b) sketch of the vegetation array, $h = 10\ cm$, $d = 0.64\ cm$ (not to scale). The blue dashed rectangular area in the inset shows the region for calculating the bulk mean values for the dense canopy case ($ah = 0.5$) with equal length to the spacing between vegetation elements. Cross signs are for ADV (upstream) and DO (downstream) locations.

Staggered configuration was chosen for the arrays. Two densities were selected to cover from sparse to dense conditions, $ah = \{0.1 - 0.5\}$ [4] (Figure 4). S_x and S_y represent the distance between elements in x-direction and y-direction, respectively, where $S_x = S_y = 5.1\ cm\ (8d)$ in the dense case, $S_x = S_y = 10.2\ cm\ (16d)$ in the sparse case.

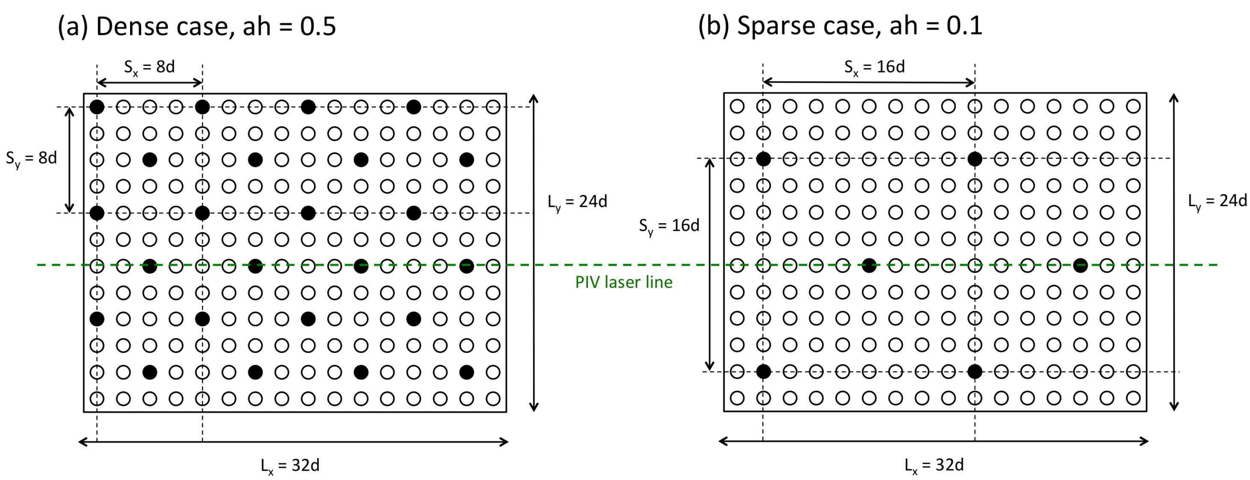

Figure 4: Staggered grid configuration of the arrays. (a) Dense case ah = 0.5. (b) Sparse case ah = 0.1. The green dashed line represents the y-location of the 2D PIV laser sheet. Black solid circles represent stem locations.

To investigate the effects of flow strength ranging from transition to fully turbulent, and submergence conditions ranging from deeply submerged to fully emergent, four mean flow velocities, and three submergence ratios, h/H, were investigated for each canopy configuration. The 28 runs, including a base case without an array, are shown in Table 2.

Table 2: Hydraulic conditions of all the experiments: the roughness density, ah , the submergence ratio, h/H, inverter frequency, f, time-averaged mean flow velocity (obtained by ADV), U, time-averaged bulk velocity (obtained by PIV), u_b, time-averaged bulk velocity within the gap, U_{gap}, $Re_H = (u_b R_H)/\nu$, $Re_d = (U_{gap} d)/\nu$, spatial calibration factor, CF, from *pixel* to *cm*, and the size of three passes used in PIVlab analysis (details in Section 2.3).

Case	*ah*	*h/H*	*f* (Hz)	*U* (cm/s)	u_b (cm/s)	U_{gap} (cm/s)	Re_H	Re_d	k_L (cm/hr)	*CF* ($cm/pixel$)	$1^{st}, 2^{nd}, 3^{rd}$ *pass size* (*pixels*)
1	0.0	0.0	10	4.27	4.45		1,715		4.71	0.007	64, 32, 16
2	0.0	0.0	20	7.50	8.16		3,271		9.66	0.007	128, 64, 32
3	0.0	0.0	30	10.76	12.14		4,887		25.38	0.007	128, 64, 32
4	0.0	0.0	40	13.77	17.22		6,737		45.61	0.007	128, 64, 32
5	0.1	0.25	10	6.03	5.60	2.45	3,562	156	3.59	0.021	64, 32, 16
6	0.1	0.25	20	12.10	11.24	4.85	7,137	308	11.81	0.021	64, 32, 16
7	0.1	0.25	30	17.33	15.82	7.86	10,378	499	27.63	0.021	128, 64, 32
8	0.1	0.25	40	22.05	19.34	6.31	13,283	401	58.48	0.021	128, 64, 32
9	0.1	0.5	10	3.97	4.50	2.96	2,467	188	3.83	0.012	64, 32, 16
10	0.1	0.5	20	8.50	8.22	5.47	4,720	347	8.93	0.012	64, 32, 16
11	0.1	0.5	30	13.31	12.31	7.81	7,075	496	28.14	0.012	128, 64, 32
12	0.1	0.5	40	18.86	16.26	10.39	9,392	660	55.90	0.012	128, 64, 32
13	0.1	1.0	10	3.40	2.86	2.86	1,241	182	4.56	0.007	64, 32, 16
14	0.1	1.0	20	5.94	5.02	5.02	2,331	319	10.62	0.007	64, 32, 16
15	0.1	1.0	30	8.52	6.15	6.15	3,201	391	24.40	0.007	128, 64, 32
16	0.1	1.0	40	11.76	8.49	8.49	4,331	539	56.05	0.007	128, 64, 32
17	0.5	0.25	10	5.45	5.74	1.23	3,395	78	5.16	0.020	64, 32, 16
18	0.5	0.25	20	10.75	10.82	2.73	6,580	174	11.31	0.020	64, 32, 16
19	0.5	0.25	30	14.40	14.79	4.33	9,418	275	26.14	0.020	64, 32, 16
20	0.5	0.25	40	20.04	18.81	5.48	12,270	348	61.46	0.020	128, 64, 32
21	0.5	0.5	10	3.80	3.58	1.37	1,942	87	4.11	0.011	64, 32, 16
22	0.5	0.5	20	7.41	7.39	3.01	3,947	191	14.19	0.011	64, 32, 16
23	0.5	0.5	30	10.31	9.90	4.17	5,596	265	26.81	0.011	128, 64, 32
24	0.5	0.5	40	14.16	15.06	7.03	7,967	446	55.07	0.011	128, 64, 32
25	0.5	1.0	10	1.75	1.01	1.01	582	64	2.35	0.006	64, 32, 16
26	0.5	1.0	20	3.86	2.13	2.13	1,185	135	6.56	0.006	64, 32, 16
27	0.5	1.0	30	4.99	3.37	3.37	1,816	214	14.42	0.006	128, 64, 32
28	0.5	1.0	40	6.64	3.79	3.79	2,269	240	42.23	0.006	128, 64, 32

2.2. Mean velocity calibration

An ADV was used to measure the mean velocity profile on the upstream side of the cylinder array. 10 vertical locations were chosen evenly distributed in a range of 0.5 cm above the bed to 5 cm below the water surface. Each measurement was recorded for 1 $minute$ at 100 Hz. The time- and depth-averaged velocity was used as the mean flow velocity corresponding to different inverter frequencies. The calibration is discussed in Section 3.1.

2.3. Flow-vegetation hydrodynamics

A 5-Megapixel CCD Camera, JAI GO-5000M-USB3, with a Navitar 25 mm focal length was used to capture images for PIV. A 5 W continuous wave laser system was used to generate a planar light sheet, with a thickness of < 1 mm at the centerline of the flume. The light sheet covers the whole observation gap (12 d) for PIV measurement (the inset in Figure 3). $8 - bit$ grayscale images were captured at 60 Hz for 1 $minute$ (3600 images) for each run. Images were processed in PIVlab [48] with a series of preprocessing methods (high pass filter, intensity capping, and contrast limited adaptive histogram equalization). Three consecutive 50% size passes with 50% overlapped interrogation areas were used to obtain higher resolution results during cross correlation calculation, while the subwindow size of the first pass followed the one quarter rule [16] (Table 2).

2.4. Interface gas transfer rate measurement

Surface gas transfer rates were determined by measuring DO concentration in water according to the methodology proposed by the American Society of Civil Engineers [43]. Cobalt Chloride Hexahydrate ($CoCl_2 \cdot 6H_2O$) was put into water as a catalyst to mix with Sodium Sulfite (Na_2SO_3), which was used as an oxygen depletion agent. More details of the DO depletion chemical process can be found in Appendix A. Once DO concentration went down to its minimum level near zero, the re-aeration process started to take place. The whole re-aeration process was monitored with a DO sensor (PASCO) at sampling intervals from 5 to 30 seconds depending on the total re-aeration time, to monitor DO, temperature, and pressure. The recovery curve of DO concentration under various vegetated flow conditions can thus be fitted based on Equation 4 to obtain the corresponding surface gas transfer rate. Results are described in Section 3.3

3. Experiment result

3.1. Flow velocity calibration

Figure 5 shows a linear increment between the inverter frequency, f, and mean flow velocity, U. When ah or h/H increases, a larger drag exerted by the vegetation reduces U, as captured by milder slopes of the fitting lines. The calibration provides a rough estimate of the mean velocities through the vegetated patch based on the inverter frequency and shows the repeatability and precise control of flow conditions on the Odell-Kovasznay flume.

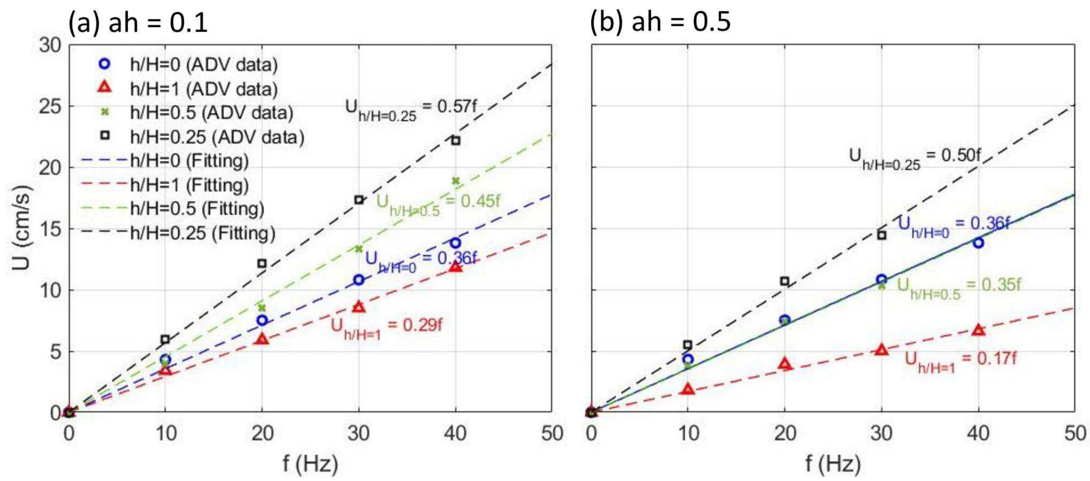

Figure 5: Mean flow velocity, U, calibration curve of the inverter frequency, f, under dense (ah $= 0.5$) and sparse configuration (ah $= 0.1$) with different submergence ratios.

3.2. Hydrodynamics

Figure 6 shows the time-averaged normalized velocity field, mean streamwise-averaged velocity profile and the streamwise evolution of velocity profiles for each case under $f = 30\ Hz$. Time-averaged bulk velocity, u_b, is used for normalization.

The flatbed case shows a typical turbulent open channel flow, with homogeneous velocity profiles in the streamwise direction (Figure 6(a)). In the emergent case ($h/H = 1$), plants exert additional drag over the whole water column, which yields lower velocity at the beginning of the gap due to proximity to the stem, and allows for flow recovery far from the vegetation. The streamwise velocity profiles are found generally constant over the entire water depth. However, an increment occurs near the bed due to the prevailing secondary flow vortex structure (horseshoe or junction vortex) that entrains fast moving fluid with high momentum from the surrounding region into the wake right behind the vegetation element, causing a velocity spike near the bed [20, 44] (Figure 6(b) and (c)).

In the submerged case, due to discontinuity of the drag at the top of the canopy, a strong shear layer is formed, which divides the flow region into two zones, above and below the penetration depth, h_p (The definition of h_p will be discussed in Section 4). When $z > h_p$ (vertical exchange zone), Reynolds stress, $\langle u'w' \rangle$, is balanced with the streamwise pressure gradient. When $z < h_p$ (longitudinal exchange zone), $\langle u'w' \rangle$ is negligible and the streamwise pressure gradient is balanced with the vegetative drag, similar to the emergent case. In this region, canopy density affects the recovery of the velocity profile, which can be seen through the comparison between Figure 6(d) and (e), (f) and (g). In addition, canopy density also determines the ratio between bottom drag and canopy drag. In the dense case, the bottom drag is much smaller than the canopy drag. Due to discontinuity of the vegetative drag, an obvious inflection point appears at the top of the canopy (Figure 6(d) and (f)). However, in the sparse case, bottom drag is comparatively important as seen in Figure 6(e) and (g), where the development of turbulent boundary layer can be seen close to the bed.

When submergence ratio $h/H = 0.5$, the canopy is under shallow submergence. The flow is confined by the limited depth, and the strong shear-layer dominates the flow structure, causing a sharper velocity gradient at the top of the canopy (see Figure 6(d) and (e)). When submergence ratio $h/H = 0.25$, the flow is not strictly confined by the water depth. Large-scale turbulent eddies start to develop and interact with the canopy-scale vortices, which causes milder velocity gradient at the top of the canopy (see Figure 6(f) and (g)).

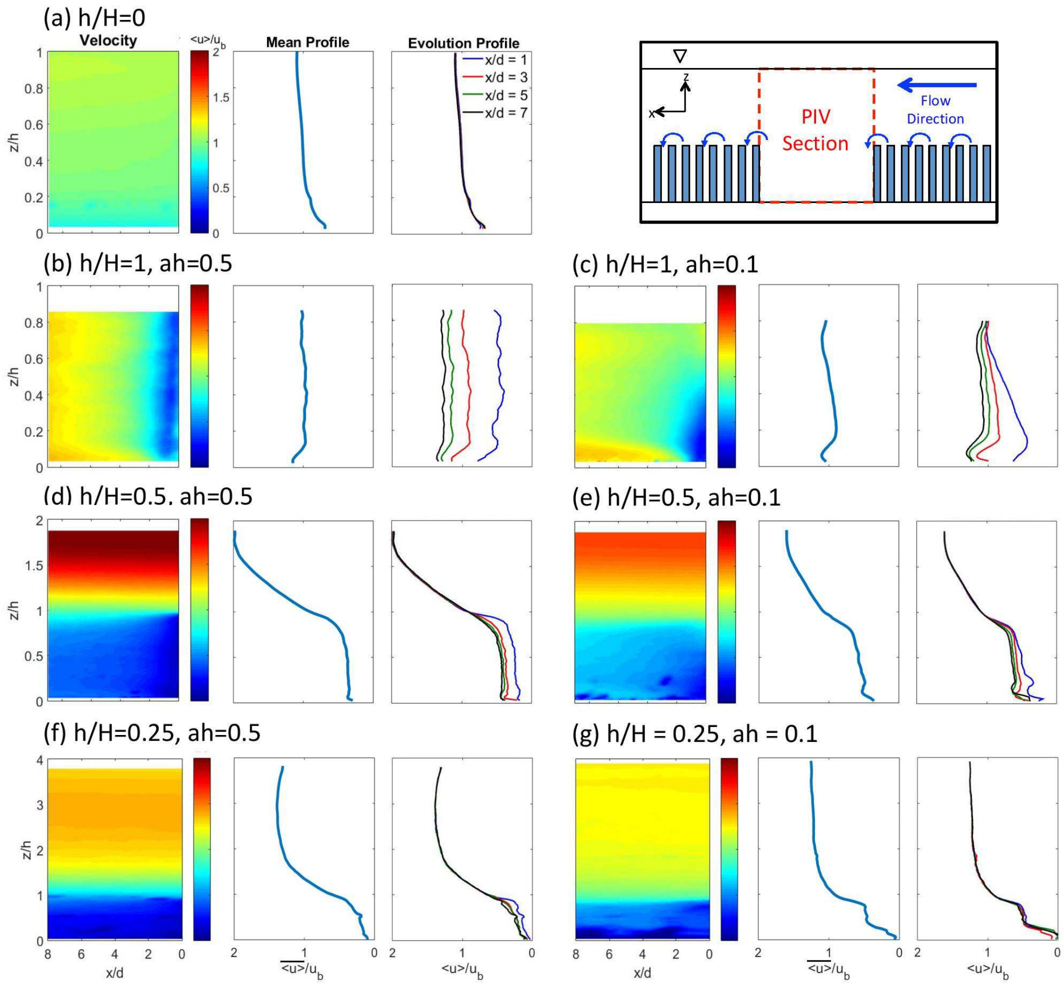

Figure 6: Normalized velocity field, mean velocity profile, and evolution profiles with different roughness density, ah, and submergence ratio, h/H, under inverter frequency $f = 30\ Hz$. Velocity is normalized by the time-averaged bulk velocity, u_b. The corresponding u_b and mean flow Reynolds number, Re_H, for cases (a)-(g) are $u_b = \{12.1;\ 3.4;\ 5.2;\ 9.9;\ 11.6;\ 14.8;\ 15.8\}\ cm/s$, and $Re_H = \{4,887;\ 1,816;\ 3,210;\ 5,596;\ 7,075;\ 9,418;\ 10,378\}$, respectively.

TKE is calculated from the PIV data as

$$TKE = \frac{1}{2}\left(2 \times \langle u'^2 \rangle + \langle w'^2 \rangle\right) . \tag{16}$$

To reduce potential errors caused by 2D-PIV data on highly 3D flows, two global filters for x- and z- components were applied to each case to remove unrealistic fluctuations. Thresholds were set as two times the largest standard deviation of instantaneous velocities u and w.

Figure 7 shows the normalized Reynolds stress field, $\langle u'w' \rangle$, TKE profiles, and the profile of mean TKE production

$$\overline{P} = -\overline{\langle u'w' \rangle \frac{\partial \langle u \rangle}{\partial z}} \tag{17}$$

(the overline represents streamwise-spatial average), with different roughness density, ah, and submergence ratio, h/H, under inverter frequency $f = 30\ Hz$. The vegetation height, h, and the characteristic shear velocity, u_c^*, are used for normalization. For the emergent case ($h/H = 1$), the bulk shear velocity, u_b^*, is used for u_c^*, which is defined as square root of the bulk Reynolds stress, while for the flatbed and the submerged cases ($h/H = 0$, 0.5, and 0.25), the maximum streamwise-averaged shear velocity, u_{max}^*, is chosen, which is defined as the maximum square root of the streamwise-averaged Reynolds stress:

$$\begin{aligned} u_c^* &= u_b^* = \sqrt{-\langle u'w' \rangle_b}\,, \quad (emergent) \\ u_c^* &= u_{max}^* = \sqrt{-\overline{\langle u'w' \rangle}_{max}}\,, \quad (flatbed\ \&\ submerged)\,. \end{aligned} \tag{18}$$

The flatbed case shows the typical turbulence properties of turbulent open channel flows in which bottom shear produces most of the turbulence in the flow. In the emergent case, the stem-scale turbulence generated by the stem elements is uniformly distributed along the z-axis. When canopy density is high, turbulence is strong near the vegetation element but decays fast away from the vegetation (Figure 7(b)). The strong TKE surrounding the vegetation makes the profile even larger than the other three local profiles $x = 3d$, $5d$, and $7d$. However, in the low density case, spatial difference is not as prominent as the dense case within the gap (Figure 7(c)). For the submerged case, a shear layer is formed at the top of the canopy, which defines the vertical penetration depth, h_p, as the z-location where Reynolds stress decays to 10% of its maximum value [29]. h_p is defined by a similar way but using mean TKE production as an indicator as shown by black dotted lines in Figure 7. Greater penetration can be observed when canopy array is sparser due to weaker shear produced at the top of canopies, which is consistent with previous studies [29]. The significant peak value of TKE production at the top of the canopy, shown in the production profiles from each case, suggests the dominance of canopy-scale turbulence compared to stem-scale turbulence in the submerged cases. Some spikes on the TKE production within the canopy shown in Figure 7(e) and (g) are due to stronger stem-scale turbulence ($Re_d > 200$) indicating the dominance of turbulent diffusion in the longitudinal exchange zone. Compared with different submergence ratios, Figure 7(d) and (e) show that under shallow submergence condition ($h/H = 0.5$), the limited water depth confines the development of the shear-layer-scale turbulence that makes the peak of TKE profile relatively non-prominent at the top of the canopy. When the submergence ratio becomes deeper ($h/H = 0.25$), the shear-layer-scale vortices are fully developed, which shows prominent TKE peak at the top of the canopy (Figure 7(f) and (g)).

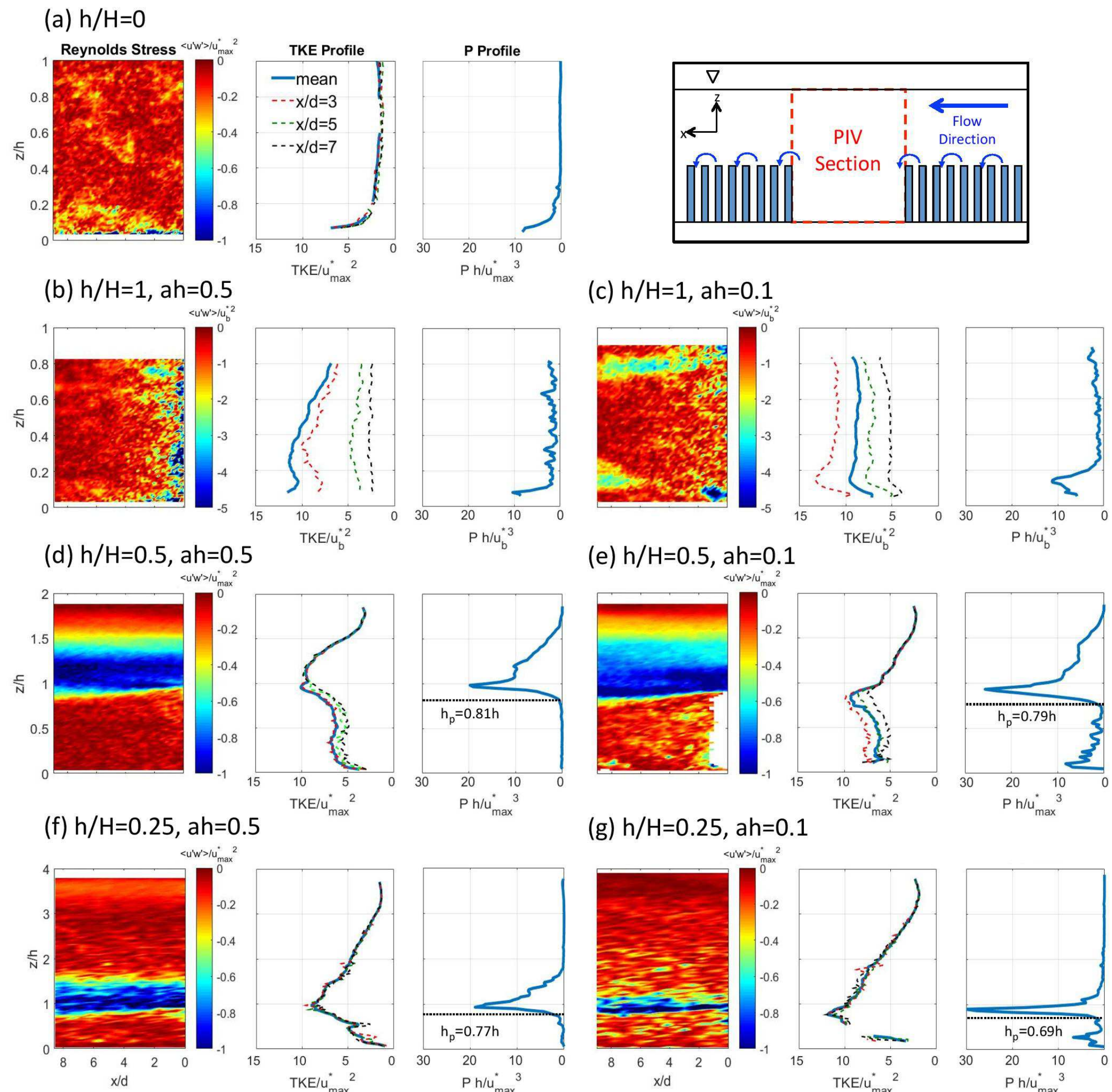

Figure 7: The normalized Reynolds stress field, TKE profiles, and mean TKE production profile with different roughness density, ah, and submergence ratio, h/H, under inverter frequency $f = 30\ Hz$. The above values are normalized by using the element height, h, and the characteristic shear velocity, u_c^*, which is set as u_b^* in the emergent cases and u_{max}^* in the flatbed and submerged cases. The corresponding u_b and mean flow Reynolds number, Re_H, for cases (a)-(g) are $u_b = \{12.1;\ 3.4;\ 5.2;\ 9.9;\ 11.6;\ 14.8;\ 15.8\}\ cm/s$, and $Re_H = \{4,887;\ 1,816;\ 3,210;\ 5,596;\ 7,075;\ 9,418;\ 10,378\}$, respectively.

By clearly presenting the distribution of the stem-scale turbulence in emergent cases, and the peak of the canopy-scale turbulence in submerged cases, mean TKE production profiles in Figure 7 shows that TKE production can be a good indicator for developing a modified surface gas transfer model to predict k_L in vegetated flows. However, an additional dispersive production, P_{dis}, is formed when doing spatial average across the canopy [21, 33] (the mean TKE production profile, $\overline{P}$). Thus, the total TKE production is given by

$$P_{tot} = \overline{P} + P_{dis} = -\overline{\langle u'w'\rangle}\frac{\overline{\partial\langle u\rangle}}{\partial z} - \overline{\langle u''w''\rangle}\frac{\overline{\partial\langle u\rangle}}{\partial z}\,, \qquad (19)$$

where $\overline{\langle u''w''\rangle}$ is the dispersive flux resulting from the spatial correlations in the time-averaged velocity field [33]. In the cases when canopy density is not extremely sparse ($ah > 0.1$), the dispersive flux can usually be neglected [17]. To test this argument, the ratio of dispersive stress to streamwise-averaged Reynolds stress, $\xi = \overline{\langle u''w''\rangle}/\overline{\langle u'w'\rangle}$, under inverter frequency $f = 30\ Hz$ for each submergence condition and canopy density is plotted in Figure 8. The dispersive fluxes only exist within the canopy due to vegetative drag exerted by the canopy elements, while the fluxes are nearly zero above the canopy in the submerged case. Among all three submergence conditions, the ratio ξ is generally within 0.1 in the dense canopy ($ah = 0.5$), while ξ is higher but still within 0.3 in the sparse cases ($ah = 0.1$). The result is generally consistent with Poggi et al. [33], who showed that dispersive fluxes can be ignored in dense canopies. However, the dispersive fluxes become increasingly significant when the canopy density becomes smaller. As shown in Figure 8, the contribution of dispersive flux does not exceed 0.3 even in the sparse cases. Hence, the mean TKE production is taken as a rough approximation of the total TKE production

$$P_{tot} \approx \overline{P} = -\overline{\langle u'w' \rangle} \frac{\overline{\partial \langle u \rangle}}{\partial z} \, . \tag{20}$$

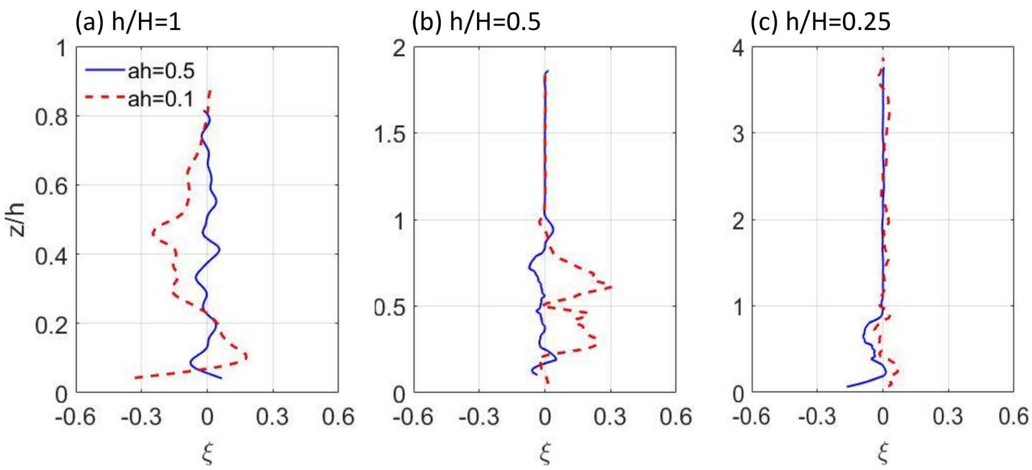

Figure 8: The ratio of dispersive stress to streamwise-averaged Reynolds stress $\xi = \overline{\langle u''w'' \rangle} / \overline{\langle u'w' \rangle}$ for different submergence ratios (a) $h/H = 1$, (b) $h/H = 0.5$, (c) $h/H = 0.25$ under inverter frequency $f = 30\ Hz$. Blue solid line represents the dense canopy case, $ah = 0.5$. Red dashed line represents the sparse canopy case, $ah = 0.25$.

Figure 9 further shows the normalized mean TKE production profiles under different inverter frequencies in each submergence condition and array density. The normalized values collapse into a single curve in each array roughness density ah and submergence ratio h/H, which provides clear turbulence characteristics for each case. In the next section, TKE production will be used to develop a modified SR model for predicting surface gas transfer rate in vegetated streams.

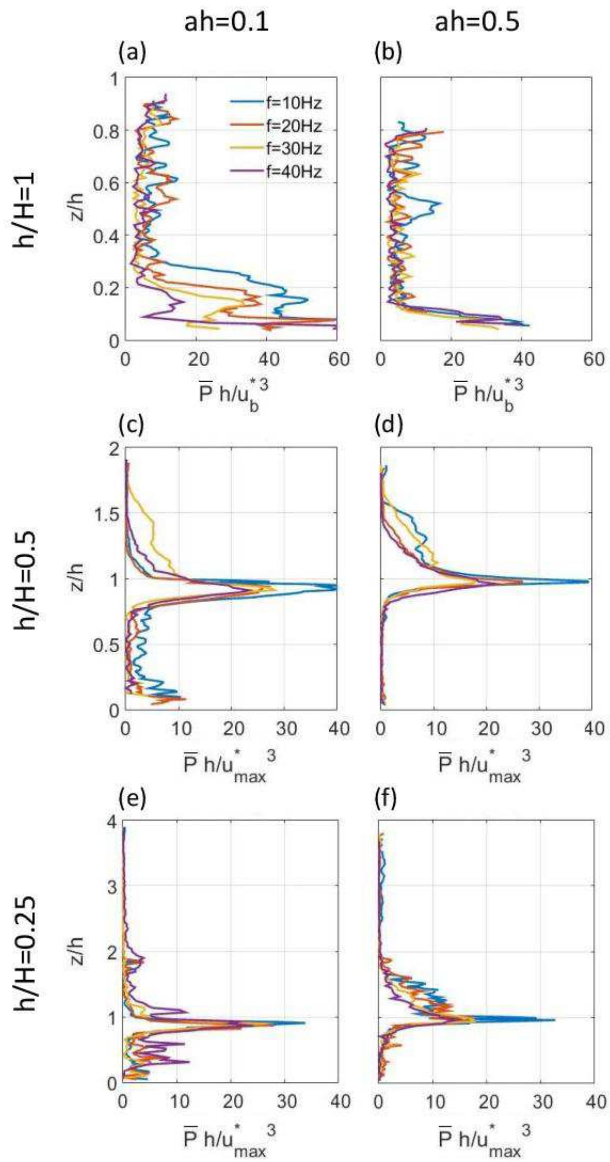

Figure 9: Normalized mean TKE production profiles under different inverter frequencies. The element height, h, and the characteristic shear velocity u_c^* are used to normalize the TKE production profile.

3.3. Gas transfer rate

Fitting DO data by Equation 4, the gas transfer rate, k_L, can be determined as shown in Figure 10, which shows the fitting results of the cases under 30 Hz inverter frequency. The fitted gas transfer rates of each case are listed in Table 2, and will be discussed in Section 4.1.

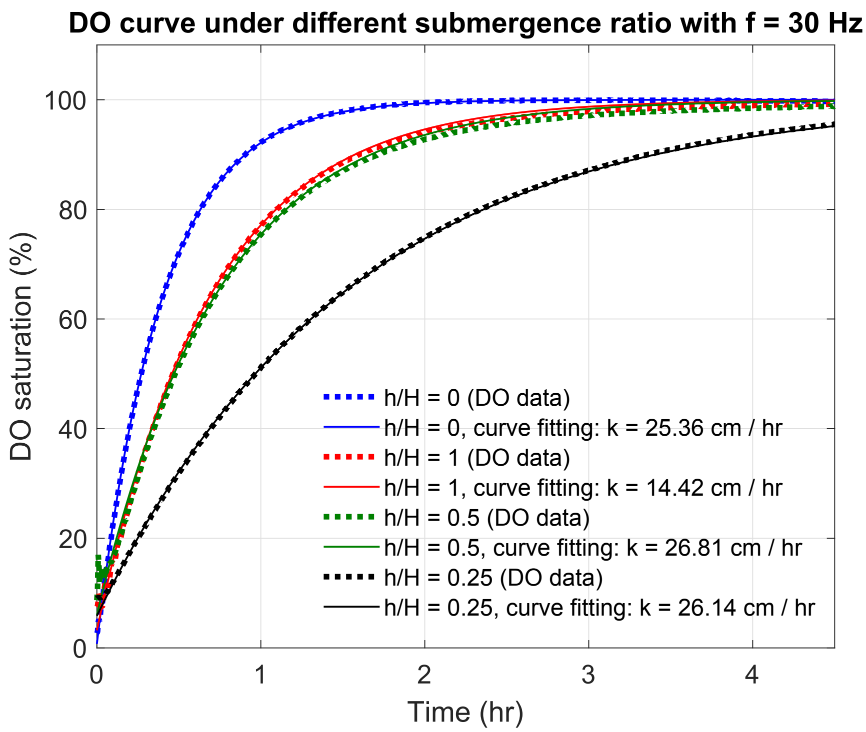

Figure 10: The fitting results of the gas transfer rate, k_L, based on Equation 4 from DO measurements under inverter frequency $f = 30\ Hz$ with $ah = 0.5$ in different submergence ratios.

4. Discussion

4.1. Surface gas transfer rate in vegetated flows

Combining hydrodynamics results from PIV data and gas transfer rate estimations from the DO test, Figure 11 shows how surface gas transfer rate, k_L, changes with the time-averaged bulk flow velocity, u_b. k_L increases faster as u_b increases in the emergent cases compared to the submerged cases. This suggests that under emergent conditions, uniformly distributed stem-scale turbulence through the entire water column enhances gas transfer more efficiently, compared to the canopy-scale turbulence generated at the top of the submerged canopy that is deeply beneath the water surface.

Also, the results show that in both emergent and submerged cases, k_L rises faster with increasing u_b for a higher array density. This outcome can be explained by turbulence strength in different submergence conditions. Under emergent conditions, the same flow velocity in the dense canopy ($ah = 0.5$) can generate stronger turbulence compared to the sparse canopy ($ah = 0.1$) (Equation 14), which enhances surface gas transfer. This happens when array density has not reached the level where the array is so dense that kills turbulence due to limited space for wake development [26, 28].

Under submerged conditions, in dense canopies ($ah = 0.5$), the canopy drag is much larger than the bottom drag, generating strong canopy-scale-turbulence at the top of the canopy. However, in sparse canopies ($ah = 0.1$), the ratio of canopy drag to bottom drag is lower, which generates weaker canopy-scale turbulence with less velocity damping than the denser canopy (Figure 7). In the sparse ($ah = 0.1$), deeply submerged ($h/H = 0.25$) case, the ratio of canopy drag to bottom drag is relatively low, and the gas transfer mechanism can be viewed as similar to the flatbed case in which turbulence is mainly generated from near the bed. Hence, we ended up with similar gas transfer rates with sparse, deeply submerged vegetation as with no vegetation for the same flow rates as shown by the black dashed line and the green line in Figure 11.

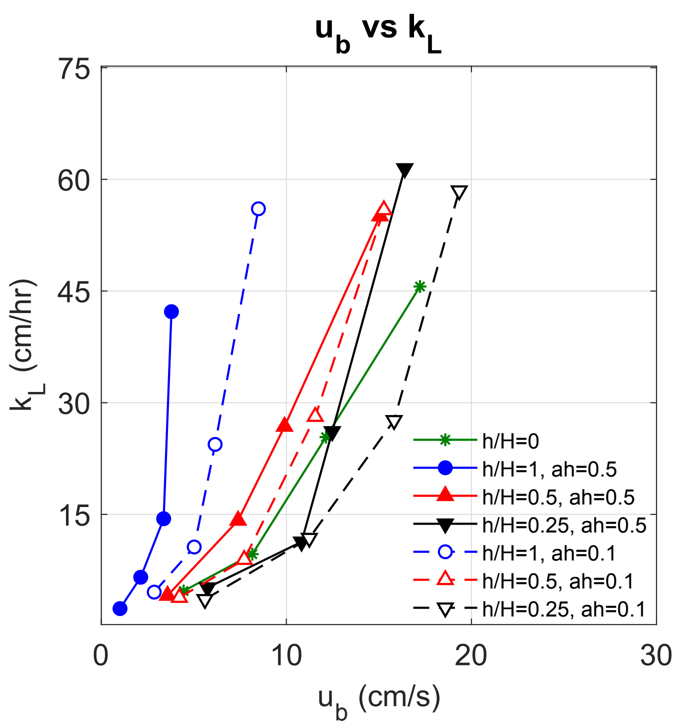

Figure 11: The relations between gas transfer rate, k_L, and the time-averaged bulk flow velocity, u_b, under different submergence ratios, h/H, and array roughness densities, ah. Solid and open symbols denote dense ($ah = 0.5$) and sparse ($ah = 0.1$) conditions, respectively.

To compare the experimental results of vegetated streams to previous field studies [51, 23, 3, 53], all measurements of k_L were normalized from $Sc = 589$ (O_2) to $Sc = 660$ (CO_2) ([52] Table 1) and plotted versus bulk flow velocity, u_b, and surface wind speed, U_w, in Figure 12. The results show two distinct regimes associated with different types of gas transfer mechanisms. One represents large-scale open water environment such as oceans, lakes, and coastal regions (previous field data), where wind forcing has long been recognized as a major factor on gas transfer. In this regime, gas transfer rate is mainly controlled by the air-side flow turbulence. Another represents small-scale shallow water systems such as streams and rivers (current experiment), where underwater turbulence is the dominant forcing that can be transported to the surface and significantly affects gas transfer [31, 39, 53, 41]. In this regime, gas transfer rate is mainly controlled by the water-side flow turbulence. Figure 12 further shows that water-side-control mechanism (current experiment) can generally induce higher k_L with lower fluid flow velocity compared to air-side-control mechanism (previous field data). Furthermore, based on different submergence ratios and canopy array densities, the response of gas transfer rate in vegetated streams as shown by the experiment data points (blue markers) can behave differently due to turbulence generated by bottom stress and vegetation as discussed previously (Figure 11).

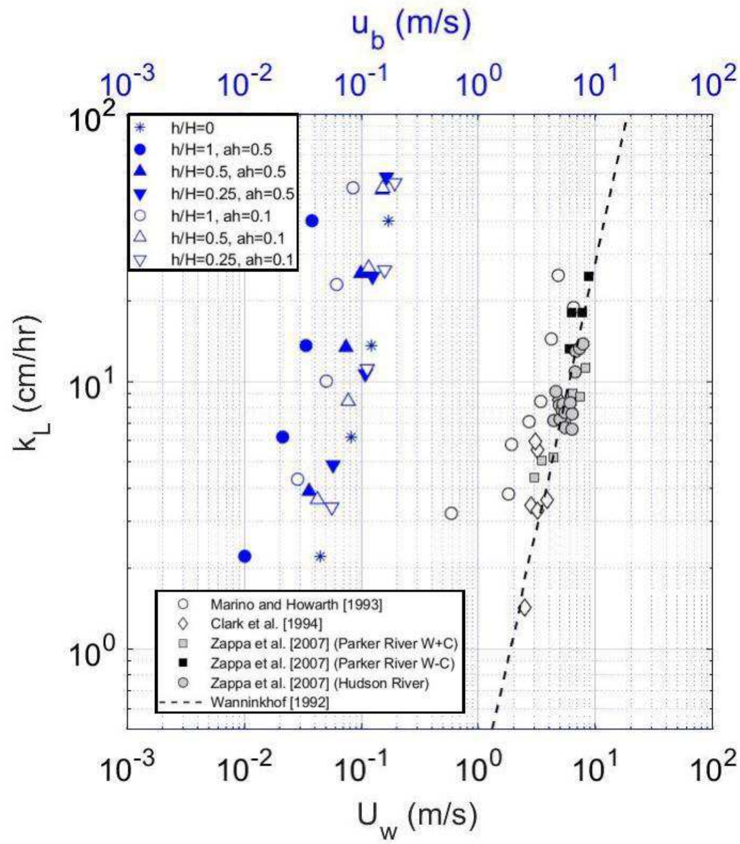

Figure 12: Gas transfer velocity versus bulk flow velocity, u_b, (blue markers; experimental results) and near-surface wind speed, U_w, (black markers; previous studies). All k_L values in the plot were normalized to $Sc = 660$ for comparison.

4.2. TKE production as a key factor on surface gas transfer process

Our data suggests that turbulence generated by the canopy can be the main driver of the surface gas transfer process in vegetated streams. Relevant turbulence statistics (e.g. TKE and Reynolds stress) and TKE budget terms (TKE production and dissipation) are commonly used to represent the strength of turbulence. According to our experimental results, TKE production is selected as the main turbulence indicator to modify the original SR model. The TKE production profiles presented in Figure 9 capture both stem- and canopy-scale turbulence characteristics in each experiment. In the emergent case, there is an uniform distribution of the vegetative drag through the entire water column, causing evenly distributed stem-scale turbulence, which suggests that bulk TKE production P_b can be used as the turbulence factor under emergent conditions. For the submerged case, canopy-scale eddies are generated by the strong shear at the top of canopy, which confines the development of stem-scale eddies within the canopy region without interacting with the free surface. The effect is similar to the blocking effect of stem-scale vortices that prevent canopy vortices interacting with the bed [29]. This suggests that the canopy-scale turbulence indicated by the prominent peak of the TKE production profile dominates vertical transport above the canopy. The maximum value of the streamwise averaged TKE production, $\overline{P}_{max}$, is then used in the modified SR model for submerged cases.

To estimate P_b and $\overline{P}_{max}$ for the emergent and submerged cases, respectively, we used time-averaged mean flow velocity, U. In the emergent case, if the conversion rate of the mean flow to the stem-scale wake generated turbulence is nearly 100%, bulk TKE production can be expressed as Equation 14 that is proportional to U^3 [38]. In the submerged case, canopy-scale turbulence is similar to the bed shear turbulence in open channel flows. Based on the definition of TKE production:

$$P = -\langle u'w' \rangle \frac{\partial U}{\partial z}\,, \tag{21}$$

a similar power-law relation between $\overline{P}_{max}$ and U is also expected. Hence,

P_b and P_{max} can be expressed as:

$$\begin{aligned} P_b &= C_{eme} U^3 \,, \\ \overline{P}_{max} &= C_{sub} U^3 \,, \end{aligned} \tag{22}$$

where C_{eme} and C_{sub} are the experimental coefficients for the emergent and the submerged cases, respectively, which can be functions of array roughness density, ah, and submergence ratio, h/H. Here, the time-averaged bulk velocity, u_b, obtained from PIV data is used as the mean flow velocity U in Equation 22. As shown in Figure 13 and Figure 14, the experimental coefficient C_{eme} is sensitive to array density in the emergent case, while submergence ratio determines the coefficient C_{sub} in the submerged case. Higher coefficient C_{eme} in the emergent case with higher array roughness density infers higher energy conversion rate from the mean flow to stem-scale turbulence through the plant stems, due to denser distribution of the vegetative drag causing stronger shear. For the submerged case, ah is not as sensitive to the experimental coefficient as the emergent case. However, the coefficient C_{sub} can change under different submergence ratio, h/H. The results suggest that higher submergence ratio has higher energy conversion rate. When the vegetation canopy is under shallow submergence conditions, the limited depth confines the development of the large-scale turbulence, which makes the canopy-scale vortices dominate the turbulence field, causing a sharper velocity gradient at the top of the canopy, compared to the deeper submergence case. Therefore, the sharper velocity gradient can lead to a higher energy conversion rate and a larger value of the coefficient C_{sub}.

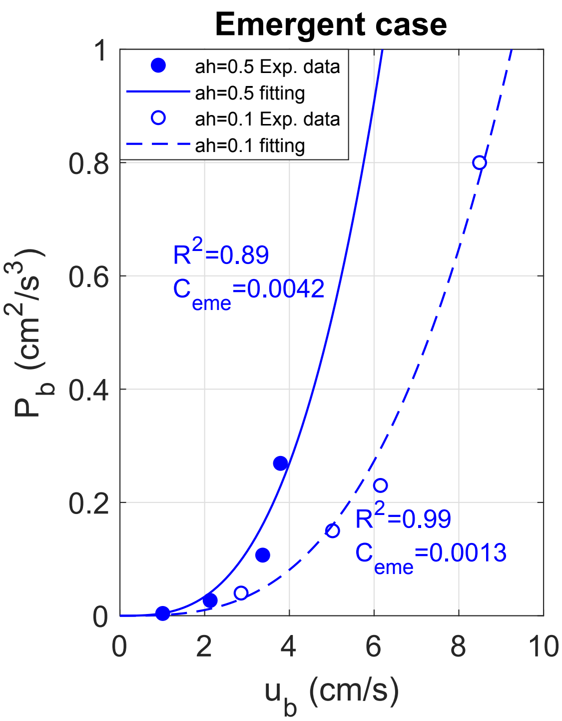

Figure 13: The relation between bulk TKE production, P_b, and the time-averaged bulk velocity, u_b, in emergent canopies. Solid dots and hollow dots represent the dense ($ah = 0.5$) and the sparse ($ah = 0.1$) case, respectively. The solid line and the dashed line represent fitting curves of the dense ($ah = 0.5$) and the sparse ($ah = 0.1$) case with 0.89 and 0.99 R-squared values, respectively.

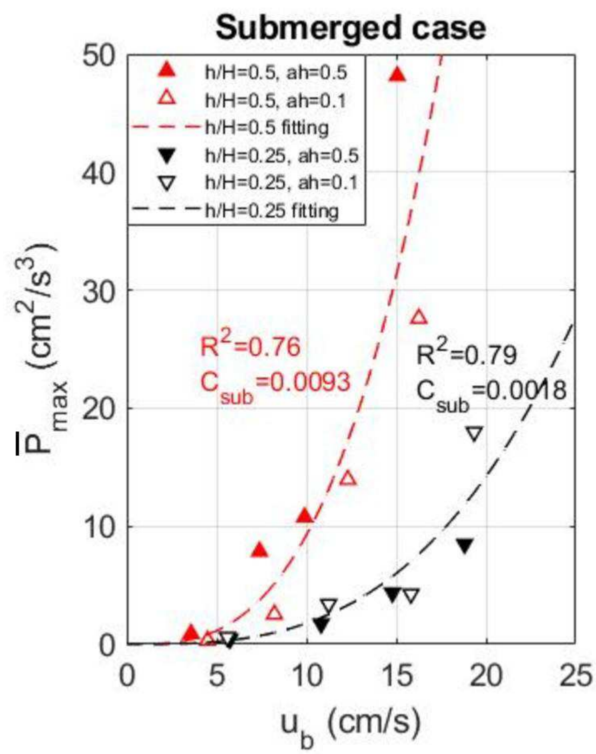

Figure 14: The relation between maximum streamwise-averaged TKE production, $\overline{P}_{max}$, and the time-averaged bulk velocity, u_b, in submerged canopies. Solid triangles and hollow triangles represent the dense ($ah = 0.5$) and the sparse ($ah = 0.1$) cases, respectively. Red upper triangles and black inverse triangles represent the cases with submergence ratio $h/H = 0.5$ and $h/H = 0.25$, respectively. The red dashed line and the black dashed line represent fitting curves of the cases under submergence ratio $h/H = 0.5$ and $h/H = 0.25$ with 0.76 and 0.79 R-squared values, respectively.

4.3. Modified SR model in vegetated flows

4.3.1. Model Derivation

To derive a new modified SR model for vegetated flows, we follow a similar normalization method for the general SD model in open channel flows proposed by Sanjou et al. [41]. The normalized SR equation can be obtained by using the characteristic shear velocity, u_c^*; molecular diffusivity, D; kinematic viscosity of water, ν; TKE dissipation rate, ϵ; and a characteristic time scale, T_c, which can be expressed as a length scale, L_c, divided by a velocity scale, U_c. The expressions for the non-dimensionalized parameters are shown as follows:

$$k_L^+ = k_L/u_c^*\,, \tag{23}$$

$$D^+ = D/\nu\,, \tag{24}$$

$$T_s^+ = T_s/T_c = (\nu/\epsilon)^{1/2}/(L_c/U_c)\,, \tag{25}$$

where the SR time scale, T_s is estimated by $(\nu/\epsilon)^{1/2}$ assuming that turbulence generated by vegetation canopies can generally be described by small-scale eddy motions. D and ν are set as 1.8×10^{-5} cm^2/s and 10^{-2} cm^2/s for water temperature $\approx 20^oC$, respectively. After non-dimensionalization, the original SR equation (Equation 5) becomes

$$k_L^+ = \alpha\sqrt{D^+/T_s^+} \rightarrow \frac{k_L}{u_c^*} = \alpha\sqrt{\frac{D}{\nu}\frac{\epsilon^{1/2}L_c}{\nu^{1/2}U_c}}\,, \tag{26}$$

where α is the experimental coefficient that depends on the flow conditions. However, the equation retains two characteristic scales, L_c and U_c, which were determined by different scales of eddies in the past [7, 2, 47]. To develop a general form that includes the information from both large-scale and small-scale eddies, the cross-scale argument of the TKE dissipation rate, ϵ, is then introduced in the model [41]. From the definition of the small eddies dissipation rate, the scaling relation is given by

$$\epsilon \approx \nu\frac{U_c^2}{L_c^2}\,. \tag{27}$$

By Tennekes and Lumley [46], the dissipation rate associated with large-scale motions can be scaled as

$$\epsilon \approx \frac{U_{le}^3}{L_{le}}\,, \tag{28}$$

where U_{le} and L_{le} are the large-scale characteristic velocity and length. In the turbulence energy cascade process, the dissipation rate should be constant from large eddies to small eddies

$$\nu \frac{U_c^2}{L_c^2} \approx \frac{U_{le}^3}{L_{le}} \rightarrow \frac{U_c}{L_c} \approx \sqrt{\frac{U_{le}^3}{\nu L_{le}}}\,. \tag{29}$$

Hence, Equation 26 can be rewritten as

$$\begin{aligned} \frac{k_L}{u_c^*} &= \alpha \sqrt{\left(\frac{\nu L_{le}}{U_{le}^3}\right)^{1/2} \epsilon^{1/2} \frac{D}{\nu^{3/2}}} \\ \rightarrow k_L &= \alpha \sqrt{\left(\frac{U_{le}^{1/2} L_{le}^{1/2}}{\nu^{1/2}} \frac{u_c^{*2}}{U_{le}^2}\right) \epsilon^{1/2} \frac{D}{\nu^{1/2}}} = \alpha \sqrt{L^+ \epsilon^{1/2} \frac{D}{\nu^{1/2}}}\,, \end{aligned} \tag{30}$$

where L^+ is the non-dimensional length scale parameter

$$L^+ = \frac{U_{le}^{1/2} L_{le}^{1/2}}{\nu^{1/2}} \frac{u_c^{*2}}{U_{le}^2} = Re_{le}^{1/2} \frac{u_c^{*2}}{U_{le}^2}\,. \tag{31}$$

4.3.2. From Surface to Bulk Flow Variables

Based on the assumption made by SR model, only molecular diffusion allows oxygen to enter the air-water interface even though turbulence indirectly acts to enhance gas transfer. Hence, traditionally, the TKE dissipation rate, ϵ, in Equation 30 needs to be determined near the water surface, which is difficult to measure directly. In fact, measuring ϵ requires high resolution PIV images to solve the derivative of turbulence fluctuations, which is another challenge for experiments especially when flow speed is high. An alternative way to obtain ϵ is from a steady-state TKE budget [32]

$$\epsilon = P - \frac{d}{dz}\langle w'q'\rangle \,, \tag{32}$$

where w' is the vertical velocity fluctuations and q' is the TKE fluctuations. The second term on the right hand side represents the turbulence transport flux derived from the triple correlation in the TKE budget, which usually can be treated as a TKE diffusion term, or T_D:

$$-\frac{d}{dz}\langle w'q'\rangle = T_D = K_t \frac{d^2 q}{dz^2} \,. \tag{33}$$

T_D is used to estimate the effect of Reynolds stress in the mean momentum equation. K_t is the eddy diffusivity, and can be estimated by various turbulence closure models. The classical Prandtl mixing-length model is adopted to calculate K_t:

$$K_t = l_m^2 \left| \frac{dU}{dz} \right| \,, \tag{34}$$

where l_m is the mixing length scale [15]

$$l_m = \begin{cases} \kappa h/3 \quad , \quad z/h < 1 \\ \kappa(z - 2h/3) \quad , \quad z/h \geq 1 \,, \end{cases} \tag{35}$$

where $\kappa = 0.4$ is the von Karman constant. As shown in Figure 15, the maximum values occur at the top of the canopy in submerged cases, while the distribution is relatively uniform throughout the whole water column in emergent cases. Two different canopy densities show similar T_D curves in all cases. However, since T_D is obtained from the second derivative of TKE, which is sensitive to any fluctuation of the profile, it also requires high resolution of the PIV images to accurately estimate its value. Figure 15 shows the characteristic curve of the T_D profile under different submergence conditions, but it also shows some fluctuation errors due to sensitivity issues. As a result, the profile is not informative enough to solve ϵ near the surface by T_D with Equation 32.

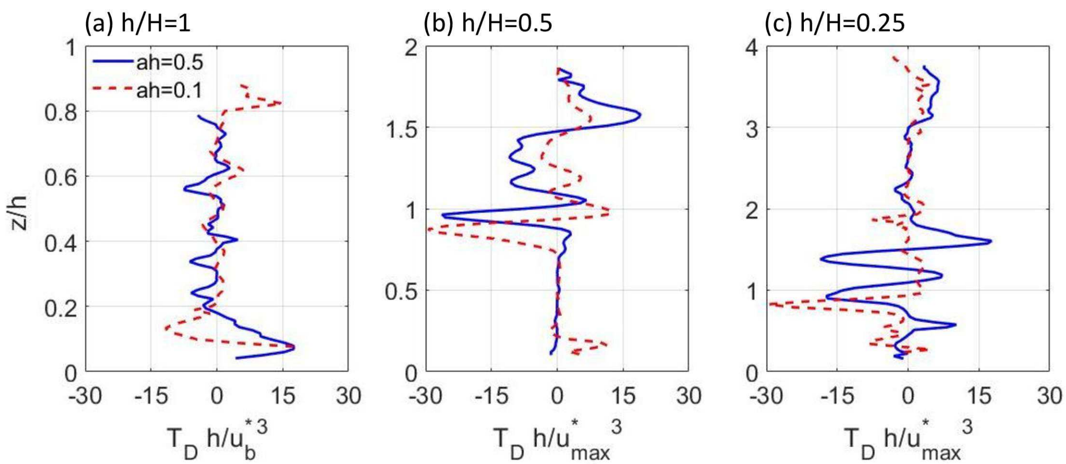

Figure 15: The normalized estimated TKE diffusion based on Prandtl mixing-length model of the vegetation canopy flows under inverter frequency $f = 30\ Hz$ for different submergence ratios (a) $h/H = 1$, (b) $h/H = 0.5$, (c) $h/H = 0.25$. Blue solid line represents the dense canopy case, $ah = 0.5$. Red dashed line represents the sparse canopy case, $ah = 0.25$.

When we treat the problem in a bulk sense, T_D plays as the inertial forces to diffuse and transport the TKE from the region where turbulence is generated toward the low turbulence locations, that is, to transport energy from large eddies to small eddies. However, the process has no effect on generating or dissipating turbulence. Hence, in a bulk sense, the problem can be narrowed down to the balance between ϵ and P, which are the main dominant terms in these scenarios. Following the argument made by Plate and Friedrich [31], that turbulence as the main factor to enhance gas transfer in open channel flow is generated through either a) the work of shearing stresses on the surface due to the action of wind, or b) at the bed due to bottom friction; and assuming that wind-induced shear on the surface can be ignored, the re-aeration TKE dissipation rate [31] can be expressed as:

$$\epsilon_{AV} = \frac{1}{L_{le}} u_c^{*2} U_{le} = \frac{{U_{le}}^3}{L_{le}} \frac{u_c^{*2}}{{U_{le}}^2} \,, \tag{36}$$

where ${U_{le}}^3/L_{le}$ can be rewritten as the large-scale characteristic TKE dissipation rate, ϵ_{cle},

$$\frac{{U_{le}}^3}{L_{le}} = \epsilon_{cle} \,. \tag{37}$$

Based on the argument of the bulk balance between the dissipation rate and the production ($\epsilon_{cle} = P_c$):

$$\epsilon_{AV} = P_c \frac{u_c^{*2}}{{u_{le}}^2} \,, \tag{38}$$

where P_c is the bulk-scale characteristic TKE production in the vegetated flow depending on the canopy submergence condition. Replacing ϵ by P_c in the previously derived non-dimensionalized SR model and combining Equation 30 and Equation 31, the final model form can be updated as:

$$k_L = \alpha \sqrt{\left(Re_{le}^{1/2} \frac{u_c^{*2}}{U_{le}^2} \right) {P_c}^{1/2} \frac{D}{\nu^{1/2}}} = \alpha \sqrt{L^+ {P_c}^{1/2} \frac{D}{\nu^{1/2}}} \,. \tag{39}$$

In summary, the whole non-dimensional derivation in Section 4.3.1 started from the traditional small-eddy SR model and then linked small-eddy dissipation to large-eddy dissipation by scaling with large-scale bulk variables U_{le}, L_{le}. Thus, local value of surface dissipation, ϵ, can be replaced by the large-scale characteristic TKE production. The bracket terms (L^+) in Equation 39 determines the constant ratio of surface small-scale dissipation to the bulk-scale dissipation. This is based on the concept that large eddies are generated by the turbulence shear (P) in vegetated flows, and energy is transported to small eddies near the water surface (ϵ) by TKE diffusion (T_D). The energy ratio between surface local scale and bulk scale is determined by the non-dimensional length scale, L^+, which is formed by the large-scale flow Reynolds number, Re_{le}, and the squared ratio of characteristic shear velocity, u_c^*, to the large-scale velocity, U_{le}.

4.3.3. Effects of Submergence Ratio

Equation 39 has provided a base of the modified SR model for vegetated flows. The remaining challenge is to properly select each bulk variable, including the bulk-scale characteristic TKE production, P_c, the characteristic shear velocity, u_c^*, and the large-scale characteristic velocity, U_{le}, and length, L_{le}. As discussed in Section 4.2, dominant TKE production values are chosen based on different submergence conditions as well as the characteristic shear velocity (see Section 3.2). In the emergent case, bulk TKE production, P_b, and bulk shear velocity, u_b^* (Equation 18), are selected for P_c and u_c^*, while the time-averaged bulk velocity, u_b, and the water depth, H, are chosen for the large-scale characteristic velocity, U_{le}, and length, L_{le}, respectively. Then, the modified SR equation for the emergent case becomes:

$$k_L = \alpha \sqrt{\left(\frac{u_b^{1/2} H^{1/2}}{\nu^{1/2}} \frac{u_b^{*2}}{u_b^2} \right) P_b^{1/2} \frac{D}{\nu^{1/2}}} = \alpha \sqrt{L_{eme}^+ P_b^{1/2} \frac{D}{\nu^{1/2}}}\,, \qquad (40)$$

where

$$L_{eme}^+ = \frac{u_b^{1/2} d^{1/2}}{\nu^{1/2}} \frac{H^{1/2}}{d^{1/2}} \frac{u_b^{*2}}{u_b^2} = Re_d^{1/2} \frac{H^{1/2}}{d^{1/2}} \frac{u_b^{*2}}{u_b^2}\,. \qquad (41)$$

The above equation shows that L^+_{eme} depends on the stem-scale Reynolds number, Re_d, the ratio of water depth to stem diameter, H/d, and the ratio of time-averaged bulk velocity to bulk shear velocity, u^*_b/u_b, which determines the constant ratio for taking bulk-scale characteristic turbulence as the indicator to predict the surface local behavior. The model equation also suggests that stem-scale turbulence generated by the emergent vegetation canopy does enhance the surface gas transfer rate, while Re_d, H/d, and u^*_b/u_b are three factors that determines how stem-scale turbulence affects surface gas transfer rates.

In the submerged case, the maximum value of the streamwise-averaged TKE production, $\overline{P}_{max}$, and the maximum streamwise-averaged shear velocity, u^*_{max} (Equation 18), are chosen for P_c and u^*_c, while the time-averaged bulk velocity, u_b, and the upper-canopy length, L_{up}, are selected for the large-scale characteristic velocity, U_{le}, and length, L_{le}, respectively. The upper-canopy length, L_{up}, is defined as the canopy-surface gap that is directly proportional to the canopy-scale vortex size [22]. Hence, the modified SR equation for the submerged case is

$$k_L = \alpha\sqrt{\left(\frac{u_b^{1/2}L_{up}^{1/2}}{\nu^{1/2}}\frac{{u^*_{max}}^2}{u_b^2}\right)\overline{P}_{max}^{1/2}\frac{D}{\nu^{1/2}}} = \alpha\sqrt{L^+_{sub}\overline{P}_{max}^{1/2}\frac{D}{\nu^{1/2}}}\,, \qquad (42)$$

where

$$L^+_{sub} = \frac{u_b^{1/2}H^{1/2}}{\nu^{1/2}}\frac{L_{up}^{1/2}}{H^{1/2}}\frac{{u^*_{max}}^2}{u_b^2} = Re_H^{1/2}\frac{L_{up}^{1/2}}{H^{1/2}}\frac{{u^*_{max}}^2}{u_b^2}\,, \qquad (43)$$

Like the emergent case, Equation 43 also shows that L^+_{sub} depends on the mean flow Reynolds number, Re_H, the ratio of upper-canopy length scale to water depth L_{up}/H, and the ratio of maximum streamwise-averaged shear velocity to time-averaged bulk velocity, u^*_{max}/u_b. It indicates that the canopy-scale turbulence generated by the submerged canopy is the main factor that enhances the surface gas transfer rate, k_L. Re_H, u^*_{max}/u_b, and the submergence ratio that determines L_{up}/H all play a role in determining k_L.

Based on the above modified SR model, Figure 16 presents the fitting results of the emergent canopy case by the model, which shows that turning points (star signs in Figure 16) occur once the stem-scale Reynolds number, Re_d, reaches 200. Since TKE production is mainly generated by the wake turbulence within the emergent canopy, when $Re_d < 200$, the wake production is relatively weak, causing turbulent component of diffusion to be negligible [26]. Hence, the coefficient α is smaller ($\alpha = 0.39$). When $Re_d > 200$, the wake production is dominant within the canopy, and the strong turbulent diffusion greatly enhances surface gas transfer, which leads to a higher α coefficient ($\alpha = 1.69$). The array roughness density, ah, is the main factor that influences the location of the turning point based on the balance between the exerted drag and the flow momentum within the canopy. As ah goes higher, the fitting line for $Re_d > 200$ is shifted toward the right due to the higher vegetative drag that reduces the flow velocity and Re_d, although with higher TKE production.

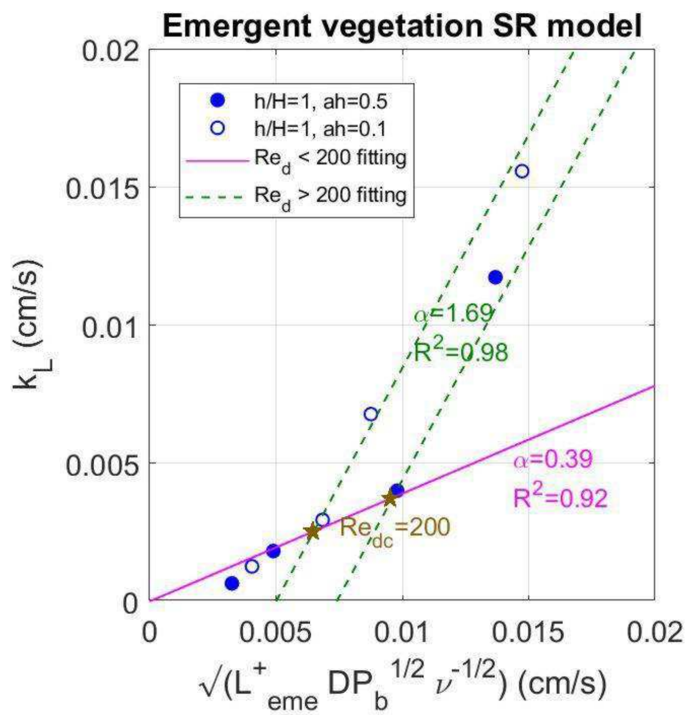

Figure 16: The linear fitting results of the emergent canopy data by the modified SR model. The critical stem-scale Reynolds number Re_{dc} is found around 200. When Re_d is below the critical value, the coefficient α is experimentally determined as 0.39 with R-squared value $R^2 = 0.92$. When Re_d is above the critical value, the coefficient α is experimentally determined as 1.69 with R-squared value $R^2 = 0.98$. The star signs represent the expected turning points ($Re_d = 200$) for each case based on the model fitting result.

On the other hand, in the submerged case, Figure 17 shows that the turning points (star signs in Figure 17) can be found when the mean flow Reynolds number, Re_H, is around $7,000$. Compared to the critical Reynolds number for transition from laminar to turbulent flow in open channel flows ($Re_H \approx 10^3$ [49]), the critical values are in the same order. This suggests that the coefficient α is related to the intermittent ejection of the shear-layer eddies at the top of the canopy into the outer stream, which can be analogous to turbulence boundary layer development of open channel flows [49], where the submerged canopy acts as bottom bed roughness. For example, Figure 6(d) and (e) show a clear difference in the velocity profile's shape between the dense case ($Re_H = 5,596 < 7,000$) and the sparse case ($Re_H = 7,075 > 7,000$) of submerged canopy flow.

By focusing on the region above the canopy, the upper canopy flow is analogous to an open channel flow with a rough bottom caused by vegetation elements. The profile in the dense case shows characteristics of the velocity profile in laminar open channel flows, while in the sparse case, the profile is close to the shape of the velocity profile in turbulent open channel flows [18], which also suggests that turbulence generation mechanism changes around $Re_H = 7,000$ in submerged cases. When $Re_H < 7,000$, canopy-scale TKE production is not dominant in the flow, and diffusion mainly comes from mechanical diffusion, causing lower α coefficient ($\alpha = 0.13$). When $Re_H > 7,000$, the turbulent canopy shear layer is fully developed, and the canopy-scale turbulence now dominates the whole diffusion process above the canopy, which makes a higher α coefficient ($\alpha = 0.71$).

Under submerged condition, the density of the canopy is not the only factor that is sensitive to the location of the turning point. Instead, submergence ratio, h/H, also plays as an effective factor because it determines both the development of the canopy-shear layer based on the above canopy length, L_{up}, and the ratio of the canopy region (drag region, where plants pose drag to the flow) to the free-flow region. When h/H is higher, sharper velocity gradient generated at the top of the canopy gives higher canopy-scale TKE production, and higher ratio of the drag/free-flow region reduces the flow velocity even more, which shifts the fitting line for $Re_H > 7,000$ toward the right to reach the critical value.

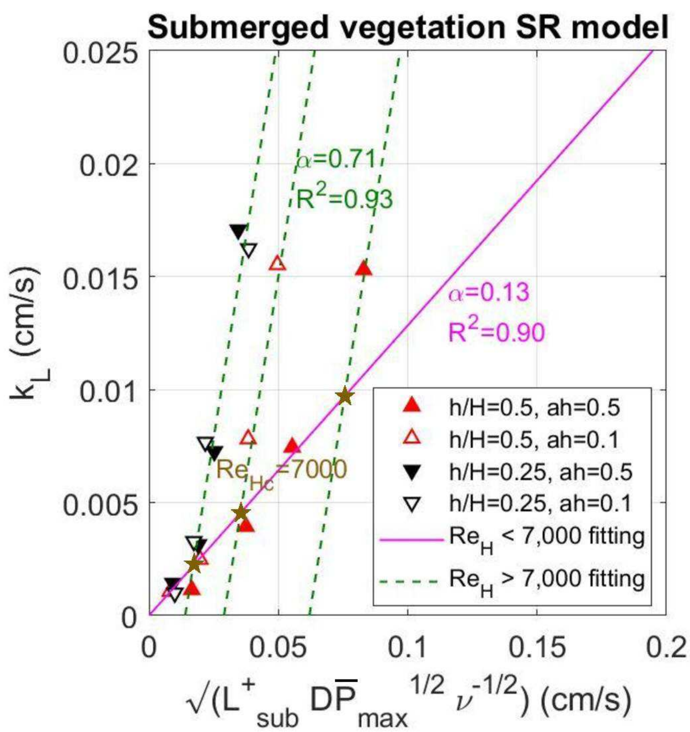

Figure 17: The linear fitting results of the submerged canopy data by the modified SR model. The critical mean flow Reynolds number, Re_{Hc}, is found around $7,000$. When Re_H is below the critical value, the coefficient α is experimentally determined as 0.13 with R-squared value $R^2 = 0.90$. When Re_H is above the critical value, the coefficient α is experimentally determined as 0.71 with R-squared value $R^2 = 0.93$. The star signs represent the expected turning points ($Re_H = 7,000$) for each case based on the model fitting result.

The R-squared values of the fitting curves are all over 0.9, which shows that the modified SR model is in a good level of effectiveness for predicting surface gas transfer rates in vegetated flows under different array densities and submergence conditions.

5. Conclusions

Our study showed that TKE production can be used as an indicator to more accurately predict surface gas transfer rates in vegetated streams. By measuring the basic vegetation and flow parameters such as ah, h/H, and U, we developed a new SR model that provides superior estimates of surface gas transfer rates, which are necessary for water quality management. Furthermore, the study provides better understanding of the magnitude and causes of variation in gas transfer velocity in vegetated rivers. Our approach can improve the accuracy of models estimating global mass balance of gases in rivers with the presence of vegetation.

The model combines the information from both large-scale and small-scale eddies. It further includes essential parameters' information of the plant canopy flow to link bulk turbulence quantities to surface motions. Based on the experimental results, we identified two critical Reynolds numbers for the emergent and submerged canopy cases, respectively, with different slopes of the linear relation between the turbulence strength and the surface gas transfer rate, which are concluded as follows:

- If the vegetation is emergent, stem-scale turbulence generated by the wake vortices is the main driver to enhance the surface gas transfer process. When stem-scale Reynolds number $Re_d < 200$, the stem-scale turbulent diffusion is relatively weak compared to mechanical diffusion in the flow, causing low enhancement of surface gas transfer. However, when stem-scale Reynolds number $Re_d > 200$, the wake production is dominant within the canopy, and the strong turbulent diffusion greatly enhances surface gas transfer rates. The array density can influence the corresponding TKE production to the value of critical Reynolds number based on the balance between the exerted drag and the flow momentum within the canopy. Higher array density results in stronger TKE production to reach the critical value, Re_{dc}, due to the higher vegetative drag that reduces the flow power.

- If the vegetation is submerged, canopy-scale turbulence generated by the sharp velocity gradient on top of the canopy becomes the dominant factor that intensifies the surface gas transfer process, compared to stem-scale turbulence that is confined within the vegetation array. The critical mean flow Reynolds number, Re_{Hc}, occurs around $7,000$. When $Re_H < 7,000$, canopy-scale TKE production is relatively weak, and diffusion mainly comes from mechanical diffusion, leading to a relatively insensitive linear relation between $\overline{P}_{max}$ and k_L. When $Re_H > 7,000$, the fully developed turbulent canopy shear layer causes canopy-scale TKE production to dominate the whole diffusion process above the canopy, resulting in a stronger coupling between $\overline{P}_{max}$ and k_L. In addition to the array density, submergence ratio, h/H, also becomes important, as it determines the development of the canopy-shear layer based on the above canopy length, L_{up}, and the ratio of the free-flow region to the canopy region, where plants pose drag to the flow. Higher submergence ratio, h/H, leads to a sharper velocity gradient generated at the top of the canopy due to limited above-canopy region. It reduces flow power more efficiently by having a relatively larger portion of the flow experiencing vegetated drag, which makes higher TKE production corresponding to the critical mean flow Reynolds number, Re_{Hc}.

Our study provides fundamental insight on how turbulence generated by aquatic vegetation affects the surface gas transfer mechanism in stream systems with changing plant densities and submergence ratios. However, the gas transfer process and the flow structure become more complex in the field, where organic sediments are present in natural systems. Such complexities include sediment transport mechanisms and biochemical effects from organic sediments interacting with vegetation and DO. Hence, more experimental studies are required to quantify such effects in the future, which is the next step of this research.

Acknowledgments

CT acknowledges funding support from Taiwan-UIUC Fellowship. This study was supported by NSF through CAREER EAR 1753200. Any Opinions, findings and conclusions or recommendations expressed in this material are those of the authors and do not necessarily reflect those of the National Science Foundation. The authors are grateful to the editors and three anonymous reviewers for their thoughtful and constructive comments on improving and clarifying the article.

Appendix A. Oxygen depletion chemical process

The American Society of Civil Engineers (ASCE) presents a guideline of an oxygen depletion method [43]. Cobalt Chloride Hexahydrate ($CoCl_2 \cdot 6H_2O$) was first put into water as a catalyst in an amount of 0.2 mg/L that is twice the amount required per litter listed in ASCE guideline. Then put

Sodium Sulfite (Na_2SO_3) into the flume as an oxygen depletion agent that reacts with DO based on the reaction:

$$2Na_2SO_3 + O_2 \rightarrow 2Na_2SO_4\,. \tag{A.1}$$

The minimum required amount of Na_2SO_3 is 7.88 mg/L per concentration of 1 mg/L of DO. The saturated DO level is in a range of 7 mg/L to 10 mg/L based on the water temperature (15 ^oC to 22 ^oC) during the experiment. Therefore, by setting 9 mg/L as the saturated DO level and increasing by a factor of 30%, fully depletion of DO can be ensured. Based on different water depths in different cases, the total amount of $CoCl_2 \cdot 6H_2O$ and Na_2SO_3 can be calculated by multiplying the total volume of water. Table A.3 provides the data acquisition rate of the DO sensor and the total amount of chemicals used in the runs.

Table A.3: The amounts of chemicals used in DO measurement and the DO sensor's data acquisition rate. ah is the array roughness density, h/H is the submergence ratio, H is the water depth, f is the inverter frequency, Na_2SO_3 is the used amount of Sodium Sulfite, $CoCl_2$ is the used amount of Cobalt Chloride, SR is the data acquisition sampling rate of the DO sensor.

$Case$	ah	h/H	H (cm)	f (Hz)	Na_2SO_3 (g)	$CoCl_2$ (g)	SR (s)
1	0.0	0.0	10	10	9.44	0.08	5
2	0.0	0.0	10	20	9.44	0.08	15
3	0.0	0.0	10	30	9.44	0.08	15
4	0.0	0.0	10	40	9.44	0.08	30
5	0.1	0.25	40	10	37.77	0.33	5
6	0.1	0.25	40	20	37.77	0.33	15
7	0.1	0.25	40	30	37.77	0.33	15
8	0.1	0.25	40	40	37.77	0.33	30
9	0.1	0.5	20	10	18.88	0.17	5
10	0.1	0.5	20	20	18.88	0.17	15
11	0.1	0.5	20	30	18.88	0.17	15
12	0.1	0.5	20	40	18.88	0.17	30
13	0.1	1.0	10	10	9.44	0.08	5
14	0.1	1.0	10	20	9.44	0.08	15
15	0.1	1.0	10	30	9.44	0.08	15
16	0.1	1.0	10	40	9.44	0.08	30
17	0.5	0.25	40	10	37.77	0.33	5
18	0.5	0.25	40	20	37.77	0.33	15
19	0.5	0.25	40	30	37.77	0.33	15
20	0.5	0.25	40	40	37.77	0.33	30
21	0.5	0.5	20	10	18.88	0.17	5
22	0.5	0.5	20	20	18.88	0.17	15
23	0.5	0.5	20	30	18.88	0.17	15
24	0.5	0.5	20	40	18.88	0.17	30
25	0.5	1.0	10	10	9.44	0.08	5
26	0.5	1.0	10	20	9.44	0.08	15
27	0.5	1.0	10	30	9.44	0.08	15
28	0.5	1.0	10	40	9.44	0.08	30

Appendix B. List of symbols used in the article

$$
\begin{aligned}
Sc &= Schmidt\ number \\
Re_t &= turbulent\ Reynolds\ number \\
\langle u' \rangle_{rms} &= root-mean-square\ of\ the\ velocity\ fluctuations \\
C_w &= local\ concentration\ of\ DO\ in\ water \\
C_{DO} &= bulk\ concentration\ of\ DO\ in\ water \\
C_{sat} &= saturated\ concentration\ of\ DO\ in\ water \\
T_s &= surface\ renewal\ time\ scale \\
F &= dissolved\ oxygen\ transfer\ flux \\
D &= molecular\ diffusivity\ of\ water \\
\nu &= kinematic\ viscosity\ of\ water \\
W &= flume\ width \\
h &= canopy\ height \\
H &= water\ depth \\
d &= stem\ diameter \\
a &= volumetric\ frontal\ area \\
ah &= array\ roughness\ density \\
h/H &= submergence\ ratio \\
f &= inverter\ frequency \\
\omega &= disk\ rotational\ frequency \\
U &= time-averaged\ mean\ flow\ velocity
\end{aligned}
\tag{B.1}
$$

$$
\begin{aligned}
u_b &= time-averaged\ bulk\ flow\ velocity\ (obtained\ by\ PIV) \\
U_{gap} &= time-averaged\ bulk\ velocity\ within\ the\ canopy\ gap \\
L &= bulk\ length\ scale \\
u &= instantaneous\ streamwise\ velocity \\
w &= instantaneous\ vertical\ velocity \\
\langle u \rangle &= time-averaged\ streamwise\ velocity \\
\langle w \rangle &= time-averaged\ vertical\ velocity \\
\overline{\langle u \rangle} &= time-averaged,\ streamwise\ averaged\ velocity \\
u' &= streamwise\ velocity\ fluctuations \\
w' &= vertical\ velocity\ fluctuations \\
\langle u'w' \rangle &= Reynolds\ stress \\
\langle u'w' \rangle_b &= bulk\ Reynolds\ stress \\
\overline{\langle u'w' \rangle}_{max} &= maximum\ of\ the\ streamwise-averaged\ Reynolds\ stress \\
P &= TKE\ production \\
P_w &= stem-scale\ wake\ TKE\ production \\
P_b &= bulk\ TKE\ production \\
\overline{P} &= streamwise-averaged\ TKE\ production \\
\overline{P}_{max} &= maximum\ streamwise-averaged\ TKE\ production \\
Re_H &= mean\ flow\ Reynolds\ number \\
Re_d &= stem-scale\ Reynolds\ number \\
k_L &= gas\ transfer\ rate \\
\alpha &= experimental\ coefficient\ of\ the\ SR\ model
\end{aligned}
\tag{B.2}
$$

$$
\begin{aligned}
C_{eme} &= experimental\ coefficient\ for\ the\ emergent\ case \\
C_{sub} &= experimental\ coefficient\ for\ the\ submerged\ case \\
\epsilon &= TKE\ dissipation\ rate \\
U_c &= characteristic\ velocity\ scale \\
L_c &= characteristic\ length\ scale \\
U_{le} &= large-scale\ characteristic\ velocity \\
L_{le} &= large-scale\ characteristic\ length \\
u^* &= shear\ velocity \\
u^*_c &= characteristic\ shear\ velocity \\
u^*_b &= bulk\ shear\ velocity \\
u^*_{max} &= maximum\ streamwise-averaged\ shear\ velocity \\
L^+ &= non-dimensional\ length\ scale\ parameter \\
L^+_{eme} &= non-dimensional\ length\ scale\ parameter\ for\ the\ emergent\ case \\
L^+_{sub} &= non-dimensional\ length\ scale\ parameter\ for\ the\ submerged\ case \\
Re_{le} &= large-scale\ Reynolds\ number \\
U_{up} &= upper-canopy\ velocity \\
L_{up} &= upper-canopy\ length \\
Re_{Hc} &= critical\ mean\ flow\ Reynolds\ number \\
Re_{dc} &= critical\ stem-scale\ Reynolds\ number \\
\langle\beta\rangle_{rms} &= root-mean-square\ of\ the\ surface\ fluctuations\ divergence \\
h_p &= vertical\ penetration\ depth \\
c &= experimental\ coefficient\ of\ the\ original\ SD\ model
\end{aligned}
\tag{B.3}
$$

$$
\begin{aligned}
U_w &= near\ surface\ wind\ speed \\
Re_{le} &= large - scale\ flow\ Reynolds\ number \\
q &= TKE \\
q' &= TKE\ fluctuations \\
\langle w'q' \rangle &= turbulence\ transport\ flux \\
l_m &= mixing\ length\ scale \\
K_t &= eddy\ diffusivity \\
\kappa &= von\ Karman\ constant \\
T_D &= TKE\ diffusion \\
\epsilon_{AV} &= re - aeration\ TKE\ dissipation\ rate \\
\epsilon_{cle} &= large - scale\ characteristic\ TKE\ dissipation \\
P_c &= bulk - scale\ characteristic\ TKE\ production \\
P_{tot} &= total\ TKE\ production \\
P_{dis} &= dispersive\ production \\
\overline{\langle u''w'' \rangle} &= dispersive\ flux \\
\xi &= the\ ratio\ of\ dispersive\ stress\ to\ streamwise - averaged\ Reynolds\ stress
\end{aligned}
\tag{B.4}
$$

References

[1] Banerjee, S., 1990. Turbulence structure and transport mechanisms at interfaces. International Heat Transfer Conference Digital Library 1, 395–418.

[2] Banerjee, S., Scott, D.S., Rhodes, E., 1968. Mass transfer to falling

wavy liquid films in turbulent flow. Industrial & Engineering Chemistry Fundamentals 7(1), 22–27.

[3] Clark, J.F., Wanninkhof, R.I.K., Schlosser, P., Simpson, H.J., 1994. Gas exchange rates in the tidal hudson river using a dual tracer technique. Tellus B: Chemical and Physical Meteorology 46(4), 274–285.

[4] Coceal, O., Belcher, S.E., 2004. A canopy model of mean winds through urban areas. Quarterly Journal of the Royal Meteorological Society 130(599), 1349–1372.

[5] Danckwerts, P.V., 1951. Significance of liquid-film coefficients in gas absorption. Industrial & Engineering Chemistry 43(6), 1460–1467.

[6] Finnigan, J.J., 2000. Turbulence in plant canopies. Annual Review of Fluid Mechanics 32(1), 519–571.

[7] Fortescue, G.E., Pearson, J.R.A., 1967. On gas absorption into a turbulent liquid. Chemical Engineering Science 22(9), 1163–1176.

[8] Foster-Martinez, M., Variano, E.A., 2016. Air-water gas exchange by waving vegetation stems. Journal of Geophysical Research: Biogeosciences 121(7), 1916–1923.

[9] Ghisalberti, M., Nepf, H.M., 2004. The limited growth of vegetated shear layers. Water Resources Research 40(7), 1–12.

[10] Herlina, N., Jirka, G.H., 2008. Experiments on gas transfer at the air-water interface induced by oscillating grid turbulence. Journal of Fluid Mechanics 594, 183–208.

[11] Higbie, R., 1935. The rate of absorption of a pure gas into a still liquid during short periods of exposure. Transactions of the American Institute of Chemical Engineers 31, 365–389.

[12] Ho, D.T., Engel, V.C., Ferron, S., Hickman, B., Choi, J., j. W. Harvey, 2018. On factors influencing air-water gas exchange in emergent wetlands. Journal of Geophysical Research: Biogeosciences 123(1), 178–192.

[13] Hotchkiss, E.R., Hall, R.O., Sponseller, R.A., Butman, D., Klaminder, J., Laudon, H., Rosvall, M., Karlsson, J., 2015. Sources of and processes controlling co_2 emissions change with the size of streams and rivers. Nature Geoscience 8(9), 696–699.

[14] Katul, G., Mammarella, I., Gronholm, T., Vesala, T., 2018. A structure function model recovers the many formulations for air-water gas transfer velocity. Water Resources Research 54(9), 5905–5920.

[15] Katul, G.G., Mahrt, L., Poggi, D., C.Sanz, 2004. One- and two-equation models for canopy turbulence. Boundary-Layer Meteorology 113(1), 81–109.

[16] Keane, R.D., Adrian, R.J., 1990. Optimization of particle image velocimeters. i. double pulsed systems. Measurement Science and Technology 1(11), 1202.

[17] King, A.T., Tinoco, R.O., Cowen, E.A., 2012. A $k-\epsilon$ turbulence model based on the scales of vertical shear and stem wakes valid for emergent and submerged vegetated flows. Journal of Fluid Mechanics 701, 1–39.

[18] Kirkgoz, M.S., Ardiclioglu, M., 1997. Velocity profiles of developing and developed open channel flow. Journal of Hydraulic Engineering 123(12), 1099–1105.

[19] Liao, Q., Wang, B., 2013. Near surface turbulence and gas exchange across the air-sea interface. Topics in Oceanography 1, 21.

[20] Liu, D., Diplas, P., Fairbanks, J.D., Hodges, C.C., 2008. An experimental study of flow through rigid vegetation. Journal of Geophysical Research: Earth Surface 113(F4), 1–16.

[21] Lopez, F., Garcia, M.H., 2001. Mean flow and turbulence structure of open-channel flow through non-emergent vegetation. Journal of Hydraulic Engineering 127(5), 392–402.

[22] Mandel, T.L., Gakhar, S., Chung, H., Rosenzweig, I., Koseff, J.R., 2019. On the surface expression of a canopy-generated shear instability. Journal of Fluid Mechanics 867, 633–660.

[23] Marino, R., Howarth, R.W., 1993. Atmospheric oxygen exchange in the hudson river: Dome measurements and comparison with other natural waters. Estuaries 16(3), 433–445.

[24] McCready, M.J., Vassiliadou, E., Hanratty, T.J., 1986. Computer simulation of turbulent mass transfer at a mobile interface. AIChE Journal 32(7), 1108–1115.

[25] McKenna, S.P., McGillis, W.R., 2004. The role of free-surface turbulence and surfactants in air-water gas transfer. International Journal of Heat and Mass Transfer 47(3), 539–553.

[26] Nepf, H.M., 1999. Drag, turbulence, and diffusion in flow through emergent vegetation. Water Resource Research 35(2), 479–489.

[27] Nepf, H.M., 2012a. Flow and transport in regions with aquatic vegetation. Annual Review of Fluid Mechanics 44, 123–142.

[28] Nepf, H.M., 2012b. Hydrodynamics of vegetated channels. Journal of Hydraulic Research 50(3), 262–279.

[29] Nepf, H.M., Vivoni, E.R., 2000. Flow structure in depth-limited, vegetated flow. Journal of Geophysical Research: Oceans 105(C12), 28547–28557.

[30] Odell, G.M., Kovasznay, L.S., 1971. A new type of water channel with density stratification. Journal of Fluid Mechanics 50(3), 535–543.

[31] Plate, E.J., Friedrich, R., 1984. Reaeration of open channel flow. Gas Transfer at Water Surfaces, Springer, Dordrecht , 333–346.

[32] Poggi, D., Katul, G.G., Albertson, J.D., 2004a. Momentum transfer and turbulent kinetic energy budgets within a dense model canopy. Boundary-Layer Meteorology 111(3), 589–614.

[33] Poggi, D., Katul, G.G., Albertson, J.D., 2004b. A note on the contribution of dispersive fluxes to momentum transfer within canopies. Boundary-Layer Meteorology 111(3), 615–621.

[34] Poindexter, C.M., Variano, E.A., 2013. Gas exchange in wetlands with emergent vegetation: The effects of wind and thermal convection at the

air-water interface. Journal of Geophysical Research: Biogeosciences 118(3), 1297–1306.

[35] Prentice, I.C., Farquhar, G.D., Fasham, M.J.R., Goulden, M.L., Heimann, M., Jaramillo, V.J., Kheshgi, H.S., Scholes, C.L.R.J., Wallace, D.W.R., 2001. The carbon cycle and atmospheric carbon dioxide. Climate Change 2001: The Scientific Basis. Contribution of Working Group I to the Third Assessment Report of the Intergovernmental Panel on Climate Change, Cambridge University Press, Cambridge, UK , 183–237.

[36] Raupach, M.R., Antonia, R.A., Rajagopalan, S., 1991. Rough-wall turbulent boundary layers. Applied Mechanics Reviews 44(1), 1–25.

[37] Raupach, M.R., Finnigan, J.J., Brunet, Y., 1996. Coherent eddies and turbulence in vegetation canopies: the mixing-layer analogy. Boundary-Layer Meteorology 78, 351–382.

[38] Raupach, M.R., Shaw, R.H., 1982. Averaging procedures for flow within vegetation canopies. Boundary-Layer Meteorology 22(1), 79–90.

[39] Raymond, P.A., Cole, J.J., 2001. Gas exchange in rivers and estuaries: Choosing a gas transfer velocity. Estuaries 24(2), 312–317.

[40] Raymond, P.A., Hartmann, J., Lauerwald, R., Sobek, S., McDonald, C., Hoover, M., Butman, D., Striegl, R., Mayorga, E., Humborg, C., Kortelainen, P., 2013. Global carbon dioxide emissions from inland waters. Nature 503(7476), 355–359.

[41] Sanjou, M., Nezu, I., Okamoto, T., 2017. Surface velocity divergence model of air/water interfacial gas transfer in open-channel flows. Physics of Fluids 29(4), 045107.

[42] Shaw, R.H., Tavangar, J., Ward, D.P., 1983. Structure of the reynolds stress in a canopy layer. Journal of Climate and Applied Meteorology 22(1), 1922–1931.

[43] Stenstrom, M., 2007. Measurement of oxygen transfer in clean water: ASCE Standard, ASCE/EWRI 2-06. American Society of Civil Engineers, USA , 42.

[44] Stoesser, T., Kim, S.J., Diplas, P., 2010. Turbulent flow through idealized emergent vegetation. Journal of Hydraulic Engineering 136(12), 1003–1017.

[45] Tamburrino, A., Gulliver, J.S., 2002. Free-surface turbulence and mass transfer in a channel flow. AIChE Journal 48(12), 2732–2743.

[46] Tennekes, H., Lumley, J.L., 1972. A first course in turbulence. MIT Press , 264.

[47] Theofanous, T., Houze, R., Brumfield, L., 1976. Turbulent mass transfer at free, gas-liquid interfaces, with applications to open-channel, bubble and jet flows. International Journal of Heat and Mass Transfer 19(6), 613–624.

[48] Thielicke, W., Stamhuis, E.J., 2014. Pivlab-towards user-friendly, affordable and accurate digital particle image velocimetry in matlab. Journal of Open Research Software 2, 1–10.

[49] Trinh, K.T., 2010. On the critical reynolds number for transition from laminar to turbulent flow. arXiv preprint arXiv:1007.0810.

[50] Turney, D.E., Banerjee, S., 2013. Air-water gas transfer and near-surface motions. Journal of Fluid Mechanics 733, 588–624.

[51] Wanninkhof, R., 1992. Relationship between wind speed and gas exchange over the ocean. Journal of Geophysical Research: Oceans 97(C5), 7373–7382.

[52] Wanninkhof, R., Asher, W.E., Ho, D.T., Sweeney, C., McGillis, W.R., 2009. Advances in quantifying air-sea gas exchange and environmental forcing. Annual Review of Marine Science 1, 213–244.

[53] Zappa, C.J., McGillis, W.R., Raymond, P.A., Edson, J.B., Hintsa, E.J., Zemmelink, H.J., Dacey, J.W.H., Ho, D.T., 2007. Environmental turbulent mixing controls on air-water gas exchange in marine and aquatic systems. Geophysical Research Letters 34(10), 1–6.